

Observations of Wave Breaking Kinematics in Fetch-Limited Seas

JESSICA M. KLEISS* AND W. KENDALL MELVILLE

Scripps Institution of Oceanography, La Jolla, California

(Manuscript received 14 October 2009, in final form 2 August 2010)

ABSTRACT

Breaking waves play an important role in air–sea interaction, enhancing momentum flux from the atmosphere to the ocean, dissipating wave energy that is then available for turbulent mixing, injecting aerosols and sea spray into the atmosphere, and affecting air–sea gas transfer due to air entrainment. In this paper observations are presented of the occurrence of breaking waves under conditions of strong winds (10–25 m s⁻¹) and fetch-limited seas (0–500 km) in the Gulf of Tehuantepec Experiment (GOTEX) in 2004. An airborne nadir-looking video camera, along with a global positioning system (GPS) and inertial motion unit (IMU), provided digital videos of the breaking sea surface and position in an earth frame. In particular, the authors present observations of $\Lambda(\mathbf{c})$, which is the distribution of breaking wave crest lengths per unit sea surface area, per unit increment in velocity \mathbf{c} or scalar speed c , first introduced by O. M. Phillips. In another paper, the authors discuss the effect of processing methodology on the resulting shape of the $\Lambda(\mathbf{c})$ distribution. In this paper, the elemental method of measuring breaking crests is used to investigate the $\Lambda(\mathbf{c})$ distributions under a variety of wind and wave conditions. The integral and the first two moments of the $\Lambda(\mathbf{c})$ distributions are highly correlated with the active breaking rate and the active whitecap coverage. The computation of whitecap coverage yields a larger observational dataset from which the variability of whitecap coverage with wind speed, friction velocity, wave age, and wave slope is presented and compared to previous observations. The dependence of the active breaking rate on the spectral peak steepness is in agreement with previous studies. Dimensional analysis of $\Lambda(c)$ indicates that scaling with friction velocity and gravity, as in the classical fetch relations, collapses the breaking distributions more effectively than scaling with dominant wave parameters. Significant wave breaking is observed at speeds near the spectral peak in young seas only, consistent with previous studies. The fourth and fifth moments of $\Lambda(c)$ are related to the flux of momentum transferred by breaking waves to the underlying water and the rate of wave energy dissipation, respectively. The maximum in the fourth moment occurs at breaking speeds of 5–5.5 m s⁻¹, and the maximum in the fifth moment occurs at 5.8–6.8 m s⁻¹, apparently independent of wave age. However, when nondimensionalized by the phase speed at the peak of the local wave spectrum c_p , the maxima in the nondimensionalized fourth and fifth moments show a decreasing trend with wave age, obtaining the maxima at dimensionless speeds c/c_p near unity at smaller wave ages and moving to lower dimensionless speeds $c/c_p \ll 1$ at larger wave ages. The angular dependence of $\Lambda(\mathbf{c})$ is predominantly unimodal and better aligned with the wind direction than the dominant wave direction. However, the directional distribution of $\Lambda(\mathbf{c})$ is broadest for small \mathbf{c} and often exhibits a bimodal structure for slow breaking speeds under developing seas. An asymmetry in the directional distribution is also observed for moderately developed seas. Observations are compared to the Phillips model for $\Lambda(c)$ in the equilibrium range of the wave spectrum. Although the ensemble of $\Lambda(c)$ distributions appears consistent with a c^{-6} function, the distributions are not described by a constant power-law exponent. However, the $\Lambda(c)$ observations are described well by the Rayleigh distribution for slow and intermediate speeds, yet fall above the Rayleigh distribution for the fastest breaking speeds. From the Rayleigh description, it is found that the dimensionless width of the $\Lambda(c)$ distribution increases weakly with dimensionless fetch, $s/u_{*e} = 1.69\chi^{0.06}$, where s is the Rayleigh parameter, u_{*e} is the effective friction velocity, and the dimensionless fetch $\chi = gXu_{*e}^2$ is a function of the fetch X and gravitational acceleration g . The nondimensionalized total length of breaking per unit sea surface area is found to decrease with dimensionless fetch for intermediate to fully developed seas, $Au_{*e}^2g^{-1} = 0.25\chi^{-0.56}$, where A is the total length of breaking crests per unit sea surface area.

* Current affiliation: University of Washington, Seattle, Washington.

Corresponding author address: Jessica M. Kleiss, University of Washington, 3737 Brooklyn Ave. NE, Box 355672, Seattle, WA 98105-5672.
E-mail: jkleiss@u.washington.edu

1. Introduction

Surface wave breaking in the deep ocean is a common phenomenon that is of central importance to the dynamics of the ocean surface and the atmospheric boundary layer, as well as the development of the wave field (Banner and Peregrine 1993; Melville 1996). One method of observing wave breaking is from the visible signature of the bright patch of bubbles entrained by whitecaps. Visible observations of wave breaking are typically described by the whitecap coverage, which is the fraction of the sea surface covered with foam. Visible wave breaking generally occurs for wind speeds in excess of 3 m s^{-1} (Monahan and O’Muircheartaigh 1986), yet is difficult to quantify and predict, even in a statistical sense. Observations of visible wave breaking typically exhibit a large amount of scatter when correlated with environmental conditions (Anguelova and Webster 2006). Field observations have considered the relationship of the whitecap coverage to wind speed and wind stress (Monahan 1971; Wu 1988), surface stability (Monahan and O’Muircheartaigh 1986; Myrhaug and Holmedal 2008), sea surface temperature (Stramska and Petelski 2003), surface currents (Kraan et al. 1996; Callaghan et al. 2008a), wave field development (Xu et al. 2000; Lafon et al. 2007), the presence of swell (Sugihara et al. 2007), wave steepness (Longuet-Higgins 1978; Snyder and Kennedy 1983; Banner et al. 2000), surfactants, salinity (Monahan and Zietlow 1969), and wind speed history (Hanson and Phillips 1999; Callaghan et al. 2008b). Whitecap coverage is often classified as active whitecap coverage W_A , associated with waves that are actively breaking, or residual whitecap coverage W_B , denoting the passive foam remaining on the sea surface from previous breaking events (Bondur and Sharkov 1982; Monahan and Woolf 1989). Visible wave breaking may also be described by the breaking rate, which is the number of breaking waves passing a fixed point per unit time, or the fraction of breaking waves per wave (Thorpe and Humphries 1980; Longuet-Higgins and Smith 1983; Holthuijsen and Herbers 1986; Lamarre and Melville 1992; Babanin et al. 2001).

Whitecap coverage and the breaking rate provide bulk representations of the amount of breaking, without any indication of the scales of waves that are breaking and dissipating energy. Information about the scales of breaking waves is of fundamental importance for the development of more rational models of air–sea mass, momentum, and energy transfer and mixed layer dynamics (Sullivan et al. 2004, 2007). An improved understanding of breaking kinematics and dynamics is necessary for the development of improved wind wave models.

A number of field studies have examined the distribution of the scale of individual breaking events, rather than bulk measurements such as whitecap coverage or

breaking rate. The scale of wave breaking has historically been determined by measuring the underlying wave profile or the breaking speed. Ding and Farmer (1994) used an array of four acoustic hydrophones to track wave breaking events and reported statistics on breaking duration, velocity, spacing, and breaking probability. Mironov and Dulov (2008) used video sequences from a mast near the Black Sea to record whitecaps. By tracking the centroids of the breaking patches they obtained a speed of breaking and used the deep water dispersion relationship to determine the frequency of breaking at different scales. Banner et al. (2002) and Manasseh et al. (2006) considered scale-dependent breaking rate observations, where the wave scale was determined from collocated wave height data.

In this paper, we present spectrally resolved measurements of wave breaking based on the crest length and breaking velocity. Phillips (1985) first suggested using $\Lambda(\mathbf{c})$, the distribution of the mean total crest length of breaking waves per unit sea surface area, per unit increment of the breaking velocity $\mathbf{c} = (c, \theta)$, where c is the speed and θ is the direction of propagation. Summing over all observed breaking wave crests, $\int \Lambda(\mathbf{c}) d\mathbf{c}$ gives the mean total length of breaking per unit area of the sea surface. The breaking distribution $\Lambda(\mathbf{c})$ can be integrated azimuthally to obtain $\Lambda(c)$ as a function of speed alone:

$$\Lambda(c) = \int_0^{2\pi} \Lambda(\mathbf{c}, \theta) c d\theta. \quad (1)$$

Phillips (1985) considered an equilibrium range of wave spectra, where the three dominant source terms of wave action input S_{in} , dissipation S_{diss} , and nonlinear wave–wave interactions S_{nl} balance. In particular, he assumed that the source terms are all important in the equilibrium range. Arguing that there is no internal wavenumber scale, he proposed that each of the three source terms is proportional. From a balance with the local form of the wave–wave interaction term, he found an expression for the spectral rate of energy loss from the wave components in the equilibrium range:

$$\epsilon(\mathbf{k}) = \sigma S_{\text{diss}} = \gamma \beta^3 (\cos \theta)^{3p} \rho u_*^3 k^{-2}. \quad (2)$$

Here β and γ arise from the proportionality constants of the input and dissipation relative to the nonlinear transfers, respectively; θ is the angle between the wind and the wave components; p is a measure of the spectral spreading of the wave field; ρ is the density of water; u_* is the wind friction velocity; and $\mathbf{k} = (k, \theta)$ is the wavenumber.

From the Duncan (1981) laboratory experiments of quasi-steady breaking using a towed hydrofoil, the average rate of energy loss per unit length of front is $b\rho(c_1^5/g)$,

where b is a numerical factor estimated by Duncan from his experiments as approximately 0.06 and c_l is the local phase speed of the breaking wave, or equivalently the incoming stream speed. The dependence of the rate of energy loss on the fifth power of c_l has also been obtained by considering turbulent dissipation in unsteady breakers (Melville 1994), the energetics of the jet of plunging water (Phillips et al. 2001), inertial arguments (Drazen et al. 2008), and the redistribution of water (Gemrich et al. 2008). Taking the breaking speed as equal to the local phase speed, the average rate of energy loss per unit area by breakers with underlying phase speeds between \mathbf{c}_l and $\mathbf{c}_l + d\mathbf{c}_l$ is

$$\epsilon(\mathbf{c}_l) d\mathbf{c}_l = b\rho g^{-1}c_l^5\Lambda(\mathbf{c}_l) d\mathbf{c}_l. \tag{3}$$

Note that the total length of breaking per unit sea surface area can be expressed equivalently as a function of either the breaking velocity \mathbf{c} or the local phase speed \mathbf{c}_l , $A = \int \Lambda(\mathbf{c}) d\mathbf{c} = \int \Lambda(\mathbf{c}_l) d\mathbf{c}_l$.

In Duncan’s experiments as well as the Phillips model, the breaking speed c is used interchangeably with the local phase speed c_l . While laboratory experiments (Rapp and Melville 1990; Stansell and MacFarlane 2002; Banner and Peirson 2007) suggest that $c = \alpha c_l$, where α is in the range [0.7, 0.9], the speed of unsteady breaking in the field is a function of time and location (see also discussions in Gemrich et al. 2008; Thomson and Jessup 2009). The speed of individual breaking events in the Gulf of Tehuantepec Experiment (GOTEX) showed a self-similar decay in time when normalized by the initial speed and the time of foam patch growth (Kleiss and Melville 2010). The Phillips model relating $\Lambda(c)$ to wave energy dissipation provides a valuable framework for scaling arguments of the form of $\Lambda(c)$. However, validation of the relationship between the breaking speed and underlying local phase speed in the field requires careful attention, and is left to a future study.

Laboratory studies on breaking due to wave group focusing (Melville 1994) showed that the breaking parameter b in Eq. (3) is not a constant but is a function of a measure of the wave slope and other parameters, including the bandwidth of the wave packet (see also Rapp and Melville 1990; Melville and Rapp 1985; Banner and Peirson 2007; Tian et al. 2008). Subsequently, Drazen et al. (2008) used an inertial argument and ballistic dynamics to predict that for plunging breakers $b = b'(hk)^{5/2}$, where b' is a constant $O(1)$, h is the height of the wave at breaking, and k is the underlying wavenumber. They confirmed this result with laboratory experiments. Banner and Peirson (2007) showed that for weakly breaking waves the threshold for breaking and the breaking parameter b could be related to the rate of focusing of the wave energy.

Phillips (1985) obtained an expression for $\Lambda(\mathbf{c})$ from (2) and (3) after conversion from wavenumber k to the local phase speed c_l using the deep water dispersion relationship, $c_l^2 = gk^{-1}$, and using c and c_l interchangeably:

$$\Lambda(\mathbf{c}) = (4\gamma\beta^3)(\cos\theta)^{3p}b^{-1}u_*^3gc^{-7} \tag{4}$$

and

$$\Lambda(\mathbf{k}) = 2\gamma\beta^3(\cos\theta)^{3p}b^{-1}u_*^3g^{-3/2}k^{1/2}. \tag{5}$$

Equations (4) and (5) can be integrated azimuthally to yield the distributions as a function of the speed c or wavenumber k :

$$\Lambda(c) = (4\gamma\beta^3)I(3p)b^{-1}u_*^3gc^{-6} \tag{6}$$

and

$$\Lambda(k) = 2\gamma\beta^3I(3p)b^{-1}u_*^3g^{-3/2}k^{3/2}, \tag{7}$$

where

$$I(3p) = \int_{-\pi/2}^{\pi/2} (\cos\theta)^{3p} d\theta.$$

The Phillips formulation for $\Lambda(c)$ was proposed for wave components in the equilibrium range of the wave spectrum that extends from wavenumbers from approximately twice the spectral peak to the smallest freely traveling gravity waves. Phillips suggested that freely traveling gravity waves are suppressed when their phase speed is less than the surface drift velocity (Banner and Phillips 1974; Phillips 1985). Phillips and Banner (1974) and Wu (1975) found that the surface drift velocity is proportional to the friction velocity u_* . The equilibrium range thus occurs for $2k_p < k < gu_*^{-2}$. The presence of surface currents would decrease the upper limit. Converting from wavenumber to wave phase speed, the equilibrium range occurs for $u_* < c < 0.7c_p$.

In this study, we determine the upper limit of the equilibrium range (or the lower limit with respect to wave speed) directly from the wave spectrum. The omnidirectional wave spectrum is expected to decrease like $k^{-2.5}$ in the equilibrium range and transition to a k^{-3} dependence at higher wavenumbers in the saturation range (Romero and Melville 2010a). One-dimensional wave spectra observed by the high-frequency Riegl laser ranging system in GOTEX showed agreement with the Banner (1990) parameterization of the one-dimensional saturation spectrum, $7 \times 10^{-3} k^{-3}$. The omnidirectional

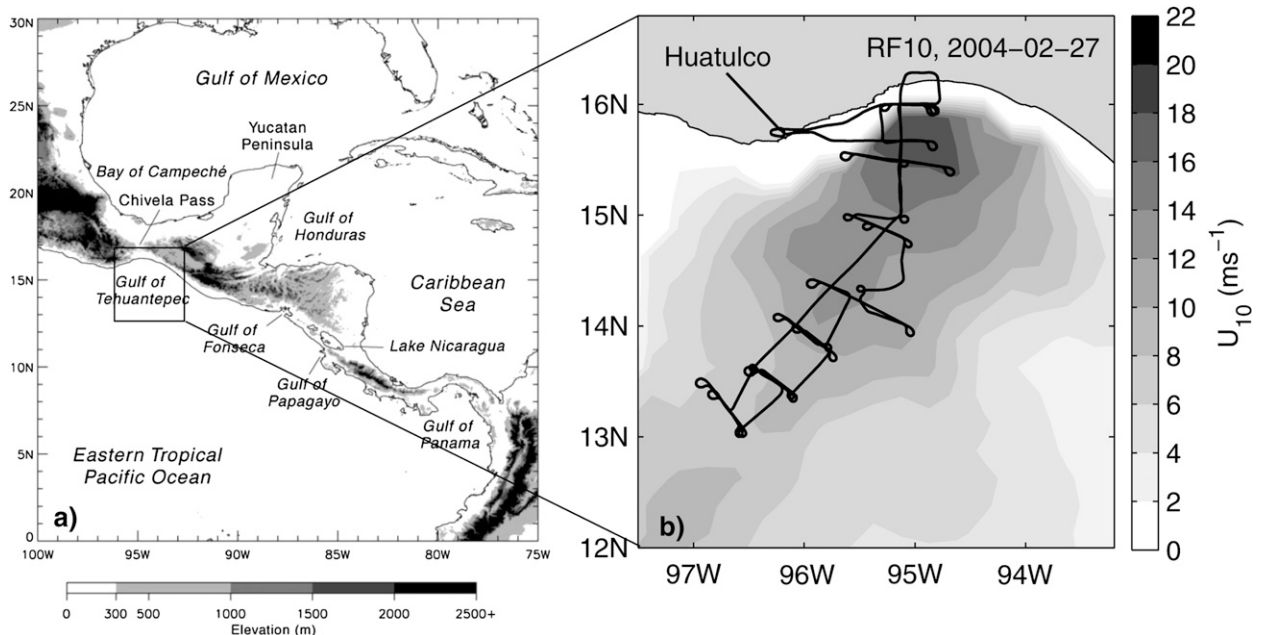


FIG. 1. (a) Map of the topography surrounding the Gulf of Tehuantepec including the Chivela mountain pass (Chelton et al. 2000). The square indicates region of inset, with flight track from research flight RF 10 shown in black and wind speed from scatterometer data shown in grayscale.

wave spectrum observed by the Airborne Terrain Mapper (ATM) scanning lidar in GOTEX showed a $k^{-2.5}$ dependence for wavenumbers above the spectral peak but did not resolve the higher wavenumbers of the saturation range. To determine the transition wavenumber k_T between the equilibrium and saturation ranges, the magnitude of the equilibrium range was determined by fitting a $k^{-2.5}$ function to the omnidirectional spectrum for wavenumbers above twice the spectral peak wavenumber. The transition wavenumber k_T is then defined where the fitted equilibrium range intercepts the function $7 \times 10^{-3} k^{-3}$.

Distributions of $\Lambda(c)$ have been observed in previous field and laboratory studies (Phillips et al. 2001; Melville and Matusov 2002; Jessup and Phadnis 2005; Gemmrich et al. 2008; Thomson and Jessup 2009; Thomson et al. 2009) using visual and infrared remote sensing of the sea surface. Kleiss and Melville (2010) give a summary of the previous studies and show that the $\Lambda(c)$ distribution is sensitive to the processing method and the definitions of breaking and breaking speed employed. The “optimal method” for the computation of $\Lambda(c)$ presented in Kleiss and Melville (2010) is summarized in this paper and applied to the full dataset from the Gulf of Tehuantepec Experiment.

In section 2, the field site and experiment are presented. The method used to compute $\Lambda(c)$ from the images described in detail in Kleiss and Melville (2010) is

summarized in section 3. In section 4, the field observations of $\Lambda(c)$, the whitecap coverage, and breaking rate are presented and correlated with the wind and wave variables. In the discussion, the observed $\Lambda(c)$ distributions are compared to the Phillips theoretical formulation, as well as to the Rayleigh distribution. The dimensionless scaling parameters that describe the $\Lambda(c)$ distributions, the total breaking length, and the width of the $\Lambda(c)$ distributions are presented as a function of the dimensionless fetch and compared to the fetch relations.

2. Experimental description

The GOTEX took place in February 2004 off the Pacific coast of southern Mexico (Fig. 1a). Typically, during the winter months from November to April, high pressure (anticyclonic) systems regularly cross over the Gulf of Mexico and create a pressure difference between the gulf and the Pacific Ocean across the Isthmus of Tehuantepec. This drives a gap flow through the Chivela mountain pass, which has an elevation of some 200 m and is flanked by the Sierra Madre, with elevations of 2000 m to the west and 1500 m to the east (Steenburgh et al. 1998). The strong northerly winds typically last 2–6 days, with winds from 10 to 25 m s^{-1} , as observed in this experiment and anecdotal reports of gusts up to 60 m s^{-1} in extreme events (Stumpf 1975). The strong winds funneled through the mountain gap then extend out over the Pacific Ocean

for 400–500 km, generally turning to the west and decreasing in speed at longer fetches (Fig. 1b). Although the strongest winds are generally associated with the Gulf of Tehuantepec, the Gulf of Papagayo and the Gulf of Panama also give rise to mountain gap winds.

These regular offshore wind jets create a natural laboratory with coastal upwelling and entrainment of cool water along the wind axis and levels of primary productivity comparable to the rich waters in the Gulf of California (Robles-Jarero and Lara-Lara 1993). Anticyclonic ocean eddies generated from the gap winds propagate up to 1500 km across the Pacific (Palacios and Bograd 2005), transporting biogenic material from the continental margin to the interior northeastern tropical Pacific (Gonzalez-Silvera et al. 2004). The site was chosen for the strong offshore flow that occurs during the gap wind events, providing the opportunity to measure and analyze the development of waves and breaking statistics in fetch-limited conditions under strong winds.

All data were collected from the NSF/National Center for Atmospheric Research C-130Q Hercules aircraft. The C130 was equipped with the standard suite of atmospheric measurements as well as an integrated optical, IR, and fixed laser altimetry system, and the NASA Airborne Terrain Mapper (ATM), a conical scanning lidar (Krabill and Martin 1987; Romero and Melville 2010a).

The measurement of breaking crest length and speed was obtained from images captured by a Pulnix TM-1040 digital video camera with a Computar 16–160-mm remotely adjustable zoom lens. The focal length was usually set to the 16-mm stop, and the focus set to ∞ . The camera captured 1 megapixel, 8-bit grayscale images at the maximum rate of 30 frames per second (fps) and recorded at a synchronized rate of either 15 or 30 fps.

Measurements of the aircraft pitch, roll, and heading from the Honeywell YG1854 Laseref SM inertial measurement unit (IMU) on board the C130 was used to determine the orientation of the camera. The camera position was obtained from the differential GPS associated with the ATM and adjusted from the GPS antenna location to the camera location. The ATM scanning lidar returned a map of the sea surface topography beneath the aircraft and also provided aircraft positioning data. From the sea surface topography, the surface wave directional spectra were estimated along with sea state parameters, including the spectral peak phase speed c_p and the significant wave height H_s (Romero and Melville 2010a). Although both wind speed and direction changed gradually with fetch, the wave energy and spectral peak frequency are in agreement with the classical fetch relations as given by Kahma and Calhoun (1992) for stable

atmospheric stratification (Romero and Melville 2010a, Fig. 7).

The wind friction velocity u_* was measured using a radome gust probe on the aircraft and Reynolds stress decomposition (Brown et al. 1983) at a height of 30–50 m above sea level. The 10-m wind speed was calculated from the friction velocity using Monin–Obukhov similarity theory (Jones and Toba 2001; Romero and Melville 2010a). The mean wind speeds used in this paper were calculated when the aircraft was flying at low altitudes and then interpolated linearly in space to yield the wind speed and friction velocity at the location of image acquisition, when the aircraft was at 400-m altitude. We assume stationarity of the wind field since the 10-min difference between wind measurements and image capture is much less than the 2–4-day time scale of the Tehuantepec wind events. However, spatial variability of the wind field on scales under 50 km is not well captured. The measured wind stress has a 35% rms error (Romero and Melville 2010a). Throughout this paper, the wave age is expressed as c_p/u_{*e} , where u_{*e} is the effective friction velocity, the component of u_* along the local dominant wave direction.

3. Methods

The full description of the method to project the images to an earth reference frame and extract the length and speed of breaking from airborne images of the sea surface is given in Kleiss (2009) and Kleiss and Melville (2010) and briefly summarized here for convenience.

The bulk translation between consecutive images of each foam patch was determined using spatial correlation and then the finescale velocity field around the perimeter was determined using optical flow. Only the component of velocity parallel to the brightness gradient is used in this analysis, as this showed the best agreement between integral properties of foam patch growth and the observed change in foam patch area. Furthermore, the breaking velocity was corrected for the effect of long wave orbital velocity on short wave breaking. The actively breaking portion of the foam patch perimeter was determined using criteria on the pointwise brightness intensity, speed, and curvature, as well as foam patch area growth. Actively breaking segments were then checked for continuity in space and time.

Thus, all breaking events were described by their perimeters, which are composed of points i , each corresponding to an arc length of the perimeter $dl_i(x, y, t)$ and a velocity $\mathbf{c}_i(x, y, t)$ with components $(c_{x,i}, c_{y,i})$. A tag indicated the segments around the perimeter that were actively breaking. The $\Lambda(\mathbf{c})$ distribution was taken as

$$\Lambda(c_x, c_y) = \frac{1}{A_{\text{TOT}}(\Delta c)^2} \sum_i \left(dl_i |c_x - \frac{\Delta c}{2} < c_{x,i} < c_x + \frac{\Delta c}{2}, c_y - \frac{\Delta c}{2} < c_{y,i} < c_y + \frac{\Delta c}{2} \right) \quad (8)$$

for all points tagged as actively breaking. Note that A_{TOT} is the total area of all overlapping images considered,¹ and differs from the total nonoverlapping sea surface observed. The bin spacing Δc is set to 0.5 m s^{-1} in this analysis. A major breaking event contributes $O(100)$ values of breaking speed $c_i(x, y, t)$ from the actively breaking points around its perimeter. The typical spread of speeds (standard deviation) for a single breaking event increases with the mean speed of breaking, from around 1 m s^{-1} for the slowest breaking events to approximately 2 m s^{-1} for mean breaking speeds above 5 m s^{-1} . The fundamental difference between Melville and Matusov (2002) and the present study is the earth referencing of the GOTEX images to an absolute reference frame, whereas Melville and Matusov defined the speed of advance of the whitecap relative to the upstream, or rear, velocity of the whitecap. Since breaking is local in space and time, it is broad in the spectral domains. Assuming a relationship of the breaking speed c to the underlying local phase speed c_l , which is related to the wavenumber and frequency, breaking should be broad in the speed domain as well.

During the GOTEX, video sequences used for kinematic processing were typically captured for a duration of 5 min at an altitude of 400 m, covering a distance of approximately 30 km. Between most image sequences, the aircraft descended to 30–50-m altitude to measure the boundary layer wind stress. The along-jet spacing between wind measurements was roughly 50 km. To have an independent wind estimate corresponding to each image sequence, it was determined that the optimal record length was one-half the image sequence, or roughly 15-km flight distance. At an aircraft elevation of 400 m, this represents roughly 3 km^2 of nonoverlapping sea surface area. On the morning of research flight RF 5, the camera focal length was inadvertently set to an unknown value. The images could not be corrected for camera lens distortion and were deemed unsuitable for breaking speed analysis. Otherwise, all image sequences obtained from a flight altitude of about 400 m that were not contaminated by sun glitter were used.

¹ A portion of each image does not overlap the sequential image due to the translation of the aircraft and must be removed from A_{TOT} because the speed of breaking cannot be computed in this region.

4. Results

a. Omnidirectional $\Lambda(c)$ distributions

The $\Lambda(c)$ distributions observed during the GOTEX campaign are shown in Fig. 2. The three analyzed research flights with image sequence locations are shown in the top row, and the corresponding $\Lambda(c)$ distributions are shown directly beneath each map. The color of the image location dot and the $\Lambda(c)$ curves indicates the effective wave age c_p/u_{*e} . The younger seas generally occur closer to shore, while more developed seas occur farther offshore. Figure 2g shows all $\Lambda(c)$ distributions together in logarithmic coordinates, along with the Phillips (1985) expression for $\Lambda(c)$ given by Eq. (6) with $b = 0.06$ and the range of estimated coefficients and observed effective friction velocities. The details of the comparison of the observations with the Phillips model are given in the discussion. Figure 2h shows the composite $\Lambda(c)$ distributions grouped according to wave age, motivated by the dimensional analysis arguments below. In order of increasing wave age, the grouped $\Lambda(c)$ distributions represent approximately 9, 15, 31, 33, and 27 km^2 of nonoverlapping sea surface area. Vertical bars show the minimum and maximum peaks of the $\Lambda(c)$ distributions in each bin.

The $\Lambda(c)$ distributions obtain a maximum in the speed range from 1 to 4 m s^{-1} . Observations at larger wave ages (red) generally show less breaking and therefore lower values of $\Lambda(c)$ than those for younger seas (blue). However, individual image sequences at intermediate development (orange) show surprisingly large estimates of breaking in research flights 5 and 7. The slight increase in the binned $\Lambda(c)$ magnitudes for the youngest seas in Fig. 2h is consistent with the variation of whitecap coverage with wave age and may be related to recent work showing that the wind stress obtains a maximum at intermediate wave ages in the range 5–15 (Nordeng 1991; Donelan et al. 1993; Makin and Kudryavtsev 2002; Lafon et al. 2007; Caulliez et al. 2008). However, the wide range of $\Lambda(c)$ magnitudes in each wave age grouping prohibits a definitive conclusion. Since the wind speed generally decreases with fetch, the magnitude of the $\Lambda(c)$ distributions may be due to a combined effect of wave state and wind speed.

The variability in the peak values of $\Lambda(c)$ and in the binned $\Lambda(c)$ distributions could have several sources. There may be other physics affecting wave breaking occurrence, such as the presence of surface currents, surface

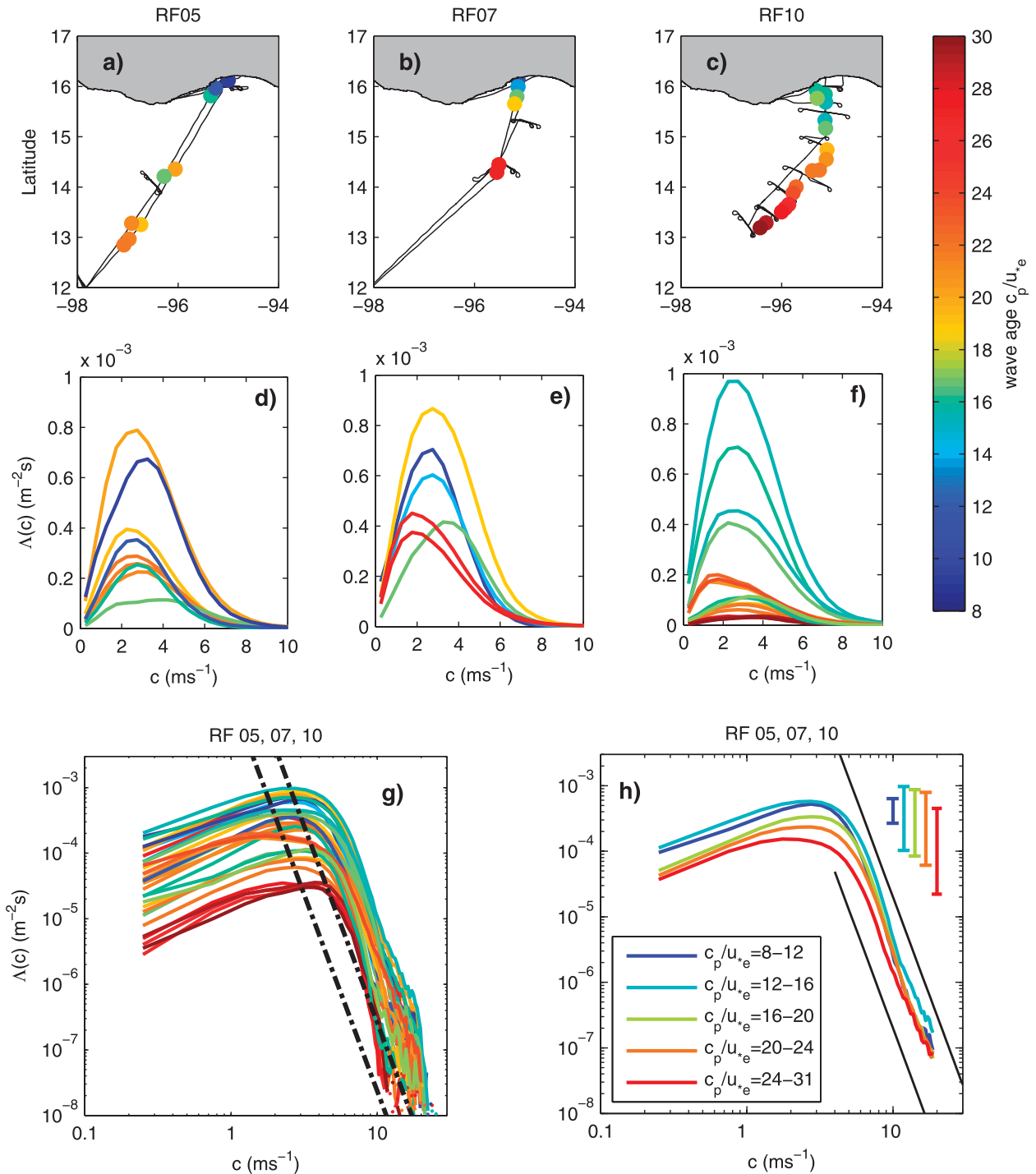


FIG. 2. The $\Lambda(c)$ distributions observed during the GOTEX. (top row) The geographic location of image sequences from (a) RF 5, (b) RF 7, and (c) RF 10. (middle row) The $\Lambda(c)$ distributions from (d) RF 5, (e) 7, and (f) RF 10. Marker color in (a),(b) and line color in (d)–(f) indicate the effective wave age c_p/u_{*e} . (bottom row) $\Lambda(c)$ distributions from all research flights presented in logarithmic coordinates. (g) The dotted–dashed diagonal lines represent the Phillips (1985) model for $\Lambda(c)$ [Eq. (6)] using $b = 0.06$, the minimum and maximum estimated coefficients of (6), and range of observed friction velocities. (h) All $\Lambda(c)$ distributions binned according to wave age as indicated in the legend. Black diagonal lines indicate a -6 power law, and error bars show the maximum range of the $\Lambda(c)$ distributions in each wave age bin.

current divergence, or air–sea instability effects. Another source of variability may come from the wind estimate. As the winds are interpolated to the image location, variability in the wind field in scales less than ~ 50 km may not be adequately reflected in the measurements. Finally, some of the scatter may be due to the amount of data used in each $\Lambda(c)$ estimate. For example, the variability of $\Lambda(c)$ is reduced significantly when the data are averaged together, as in Figs. 2g and 2h.

b. Dimensional analysis

We consider a nondimensional scaling to collapse the $\Lambda(c)$ curves in Fig. 2g. The $\Lambda(c)$ distribution has dimensions $L^{-2}\Gamma$. Assuming that the wave breaking has the same controlling parameters as the underlying wave field (as in the classical fetch relations due to Kitaigorodskii 1962), $\Lambda(c)$ may depend on (c ; ρ_a , ρ_w , u_* , g , k_p , H_s , Γ , and X), where ρ_a and ρ_w are the densities of air and water respectively, u_* is the friction velocity in air, k_p the spectral peak wavenumber, H_s the significant wave height, Γ the surface tension coefficient, and X is the fetch. Dimensional analysis then yields

$$\Lambda u_*^3 g^{-1} = f\left(\frac{c}{u_*}; \frac{gX}{u_*^2}, \frac{\rho_a}{\rho_w}, H_s k_p, \frac{k_p u_*^2}{g}, \text{Bo}\right) \quad (9)$$

where gXu_*^{-2} is the dimensionless fetch and $\text{Bo} = \Delta\rho g\Gamma^{-1}k_p^{-2}$ is the Bond number. The dimensionless group ρ_a/ρ_w is approximately constant. We assume asymptotic independence of the large Bond number because our measurements cannot resolve waves small enough to be directly affected by surface tension. Furthermore, the wave development fetch relations (Hasselmann et al. 1973), which apply here for the gross wave field parameters (Romero and Melville 2010a), present k_p and H_s as functions of g , u_* , and X , so they may be considered as secondary functions. We then have

$$\Lambda u_*^3 g^{-1} = f\left(\frac{c}{u_*}; \frac{gX}{u_*^2}\right). \quad (10)$$

In other words, the $\Lambda(c)$ distribution is expected to be a function of the dimensionless breaking speed and the dimensionless fetch, which is a measure of the wave development. This result is not unique. For example, we could choose to use the slope parameter $H_s k_p$ instead of the dimensionless fetch; however, given the fetch-limited nature of these experiments, Eq. (10) appears to be the best choice for our purposes.

The dimensionless Λ distributions generally decrease with wave age (Fig. 3a). To determine the dependence on the nondimensional fetch $\chi = gX_e u_*^{-2}$ that captures this trend, the maximum value of each (nonbinned)

nondimensional distribution $u_*^3 g^{-1} \Lambda(c/u_*)$ is determined, \hat{L}_{peak} . An empirical fit of \hat{L}_{peak} to the dimensionless fetch gives an exponential function of the form $\hat{L}_{\text{peak}} = a_1 \exp(a_2 \chi)$, with $a_1 = 1.4 \times 10^{-5}$ and $a_2 = -2.0 \times 10^{-7}$.

The $\Lambda(c)$ distributions shown in Fig. 3b are nondimensionalized by $u_*^3 g^{-1}$, scaled according to the exponential fit given above and then grouped by wave age. The nondimensionalized and scaled data in Fig. 3b agree to within a factor of 5 for $c/u_* > 7$, where u_* ranges from 0.46 to 0.80 m s^{-1} . The high breaking speed region appears to be empirically consistent with a -6 power law, shown by a thin black line in Figs. 3a,b for reference. A full comparison of the data to a -6 power law will be addressed in the discussion. The distributions in linear coordinates in Fig. 3b show that the peaks of $\Lambda(c)$ do not collapse particularly well with this scaling, although there is no trend with wave age.

Previous observations of $\Lambda(c)$ (Gemrich et al. 2008; Thomson and Jessup 2009) have reported $\Lambda(c)$ distributions normalized by wave properties such as the spectral peak phase speed c_p and the dominant wavenumber k_p . As discussed in Gemrich et al. (2008), to preserve the total length of breaking per unit sea surface area,

$$\int \Lambda\left(\frac{c}{c_p}\right) d\frac{c}{c_p} = \int \Lambda(c) dc. \quad (11)$$

It follows that $\Lambda(c/c_p) = c_p \Lambda(c)$, with units L^{-1} . This is then nondimensionalized with $k_p^{-1} = c_p^2/g$, according to the dispersion relation. The full nondimensional form is $\Lambda(c)c_p^3 g^{-1}$. Note that this is equal to the previous expression, $\Lambda(c)u_*^3 g^{-1}$, times wave age to the third power.

Figure 3c shows the $\Lambda(c)$ distributions nondimensionalized with wave parameters. The least-developed seas (blue) show $\sim 5\%$ of wave breaking at and above the spectral peak phase speed, $c/c_p \geq 1$, while the older seas show very little wave breaking at speeds faster than c_p . This is in agreement with many previous observations (Ding and Farmer 1994; Melville 1994; Felizardo and Melville 1995; Banner et al. 2000; Gemrich et al. 2008), although Thomson et al. (2009) found that the breaking distributions collapsed around $c/c_p \approx 0.4$. The magnitude of the dimensionless $\Lambda(c)c_p^3 g^{-1}$ distributions is suppressed for the young waves (blue) since c_p increases with fetch. Scaling the breaking speed with the dominant phase speed c_p does not collapse the data. In fact, it introduces a greater dependency on wave age than the original dimensional $\Lambda(c)$ distributions.

One of the major motivations for observing the $\Lambda(c)$ distribution is the relationship between the fifth moment of $\Lambda(c)$ and the rate of wave energy dissipation $\epsilon(c)$ [Eq. (3)]. The fifth moment of the omnidirectional $\Lambda(c)$,

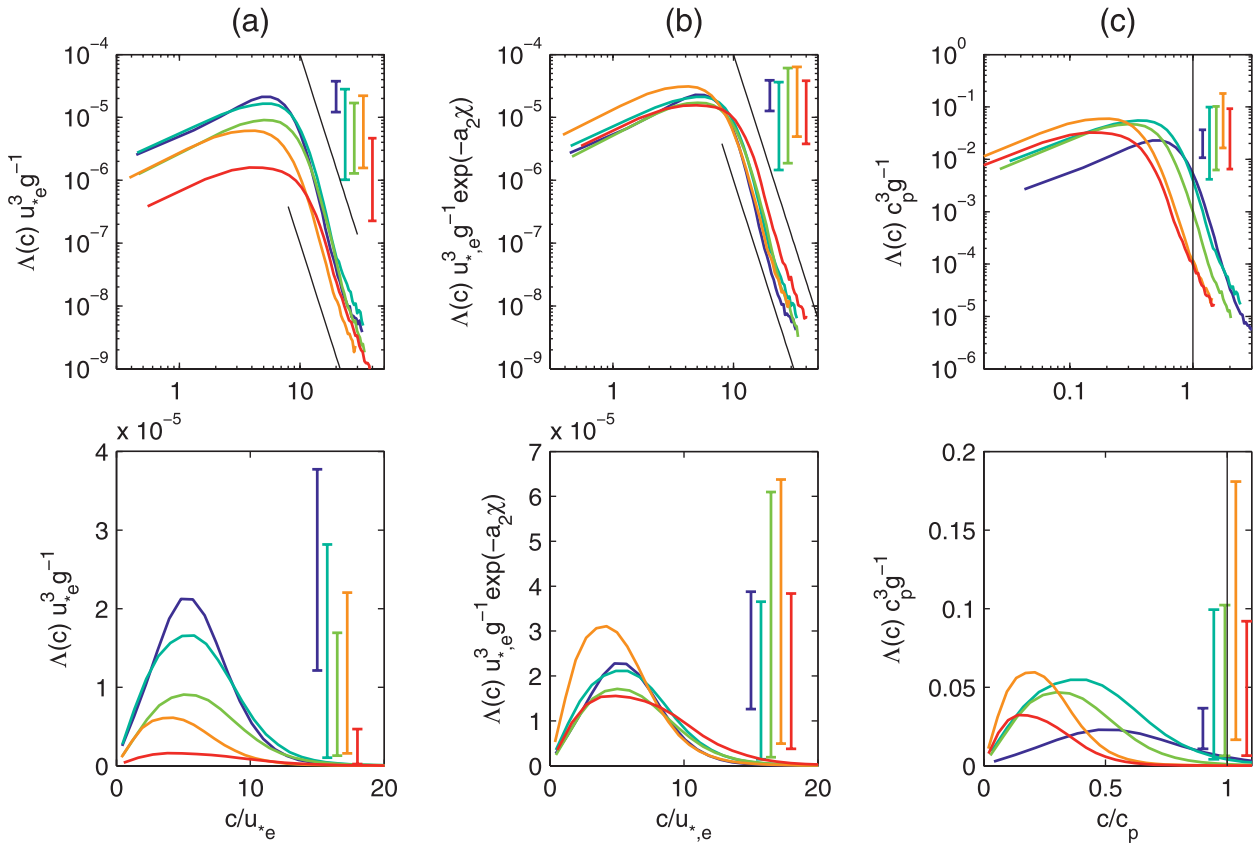


FIG. 3. The nondimensionalized $\Lambda(c)$ distributions, averaged together according to wave age c_p/u_{*e} in (top) logarithmic and (bottom) linear coordinates. Error bars show the range of maxima of the dimensionless $\Lambda(c)$ distributions within each average. (a) The breaking length distribution and breaking speed nondimensionalized by effective friction velocity and gravity. (b) $\Lambda(c)$ nondimensionalized according to Eq. (10) in which the function of dimensionless fetch χ is $\exp(2.0 \times 10^{-7}\chi)$. (c) $\Lambda(c)$ distributions nondimensionalized using dominant phase speed c_p . Diagonal black lines in (a) and (b) of (top) indicate a -6 power law function. Vertical black lines in (c) indicate where the breaking speed equals the spectral peak phase speed.

scaled with the density of water and gravity, is presented in Fig. 4 in both dimensional and nondimensional form. In Fig. 4a, the dimensional fifth moment of $\Lambda(c)$ is shown in logarithmic (top) and linear (bottom) coordinates. The binned fifth moment of $\Lambda(c)$ obtains a maximum value at speeds from 5.8 to 6.8 m s^{-1} , apparently independent of wave age. The horizontal bars in Fig. 4a (bottom) indicate the range of the spectral peak phase speed c_p within each wave age grouping.

Figures 4b and 4c show the fifth moment of the nondimensionalized breaking speeds and distributions, subsequently binned according to wave age. Figure 4b has been nondimensionalized with u_{*e} and gravity, equivalently to Fig. 3a. The nondimensionalization of the fifth moment results in a decrease in the range of the maxima from a factor of ~ 5 in the dimensional case to a factor of ~ 3 . Interestingly, when the fifth moment of $\Lambda(c)$ is nondimensionalized with the wave field parameters, Fig. 4c, a clear trend is apparent. The nondimensionalized fifth moment is greatest for the young seas with a maximum

occurring at breaking speeds around the spectral peak phase speed. As wave age increases, the magnitude of the nondimensionalized fifth moment decreases, and its maximum moves to speeds much less than the spectral peak phase speed. This suggests that there may be an approach to saturation of the fifth moment at smaller values of c/c_p (Fig. 4c).

The associated flux of momentum transferred by breaking waves to the underlying water in the direction of the wind can be expressed as

$$\tau(c) = \frac{\epsilon(c)}{c} \cos\theta, \tag{12}$$

where θ is the angle between the wind and the waves. Thus Eqs. (3) and (12) indicate that the momentum flux from breaking waves to the underlying current is a function of the fourth moment of $\Lambda(c)$. The dimensional and nondimensional fourth moment of $\Lambda(c)$ distributions appear qualitatively similar to the fifth moment (not shown). The maximum in the dimensional fourth moment of $\Lambda(c)$

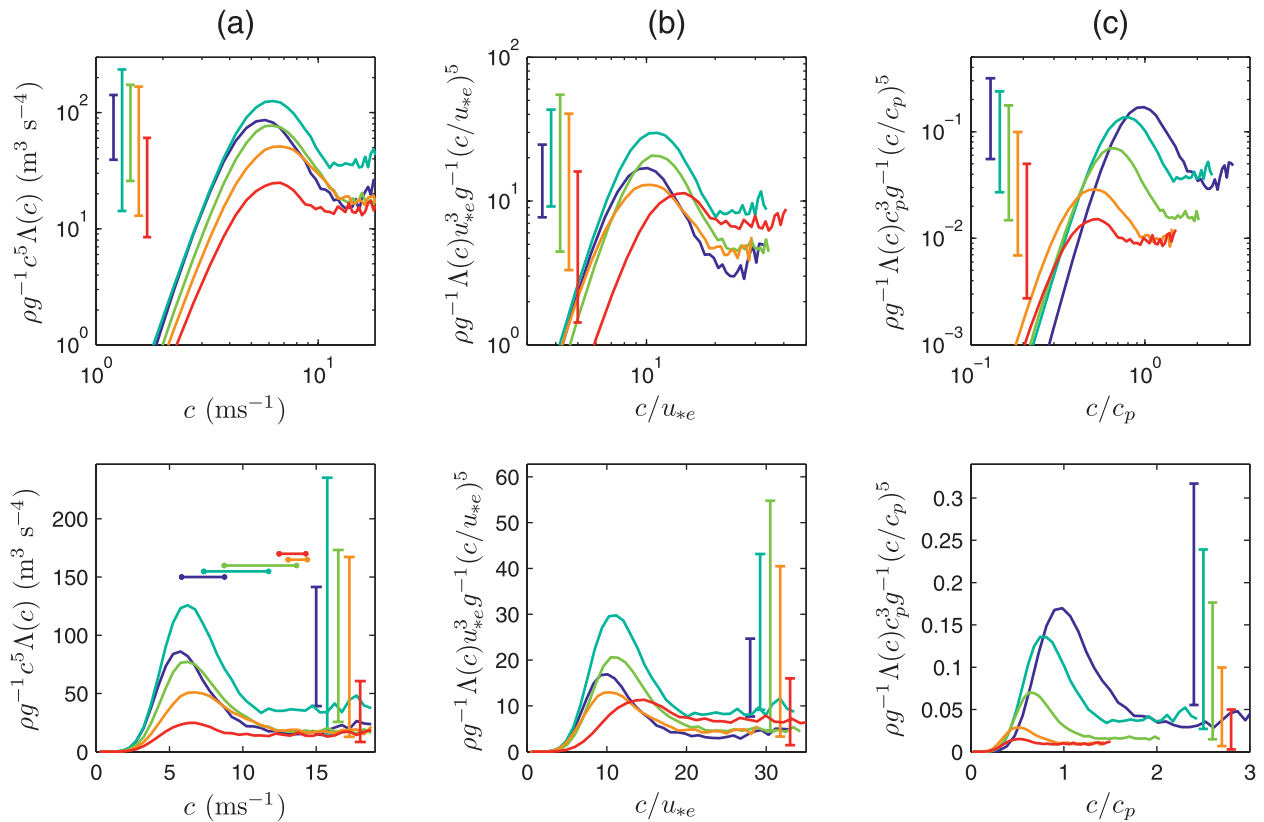


FIG. 4. The fifth moment of $\Lambda(c)$ displayed in (top) logarithmic and (bottom) linear coordinate systems. Observations are binned by wave age and averaged together (color). The breaking speed and $\Lambda(c)$ distributions are shown in (a) dimensional form and (b) nondimensionalized using effective friction velocity and gravity and (c) nondimensionalized using peak wave parameters. The vertical error bars show the range of the peaks of the distributions in each bin. The horizontal bars in (a) show the range of the spectral peak phase speed c_p within each wave age bin.

occurs at $4\text{--}20 \text{ m}^2 \text{ s}^{-3}$, at a speed of $5\text{--}5.5 \text{ m s}^{-1}$. The fourth moment nondimensionalized with u_{*e} and g appears very similar to Fig. 4b, with maximum values an order of magnitude less than the fifth moment. The fourth moment nondimensionalized with wave parameters shows the same organized trend as the fifth moment in Fig. 4c.

The fourth and fifth moments of $\Lambda(c)$ clearly demonstrate two regimes of the distribution—a smoothly varying peaked function for speeds less than 10 m s^{-1} followed by a tail that may have a power law description. The nature of these curves will be addressed further in the discussion section.

c. $\Lambda(c)$: The directional distribution

Figure 5 shows examples of the directional $\Lambda(\mathbf{c})$ distributions of six sample image sequences selected from research flight 10. The distributions are shown in earth coordinates, so $\mathbf{c} = (c_x, c_y)$ are the east and north directions, respectively. The black arrows indicate the dominant wave direction and terminate at the spectral peak phase speed. As in Fig. 3c, some wave breaking is seen at speeds of the spectral peak phase speed for the youngest seas (Figs. 5a,b),

while nearly no breaking is seen at the spectral peak phase speed for the older seas (Figs. 5d–f). The 10-m wind speed and direction is indicated by the black asterisks in each panel. For the youngest seas (Fig. 5a), we see that the wind speed is much faster than the spectral peak phase speed, and the angle between the wind velocity and the dominant wave direction is 26° . The other five examples show closer alignment between the wind and dominant waves, with Figs. 5c,d showing a difference of 8° , and the others agree to within 2° . The large angle between the wind and the dominant waves at short fetch is likely because our flight path was not directly down the center of the wind jet but to the west of it (see Fig. 1b). The waves traveling to the west of the local wind may have been radiating away from the stronger winds in the core of the wind jet.

Overlaid on each figure are concentric circles indicating the limits of the equilibrium range. The outer circle is set at $0.7c_p$, which is equal to $2k_p$ via the dispersion relationship. The inner circle indicates the phase speed of the wave component at which the omnidirectional spectrum transitions from a power-law slope of -2.5 to -3 (Romero and Melville 2010a).

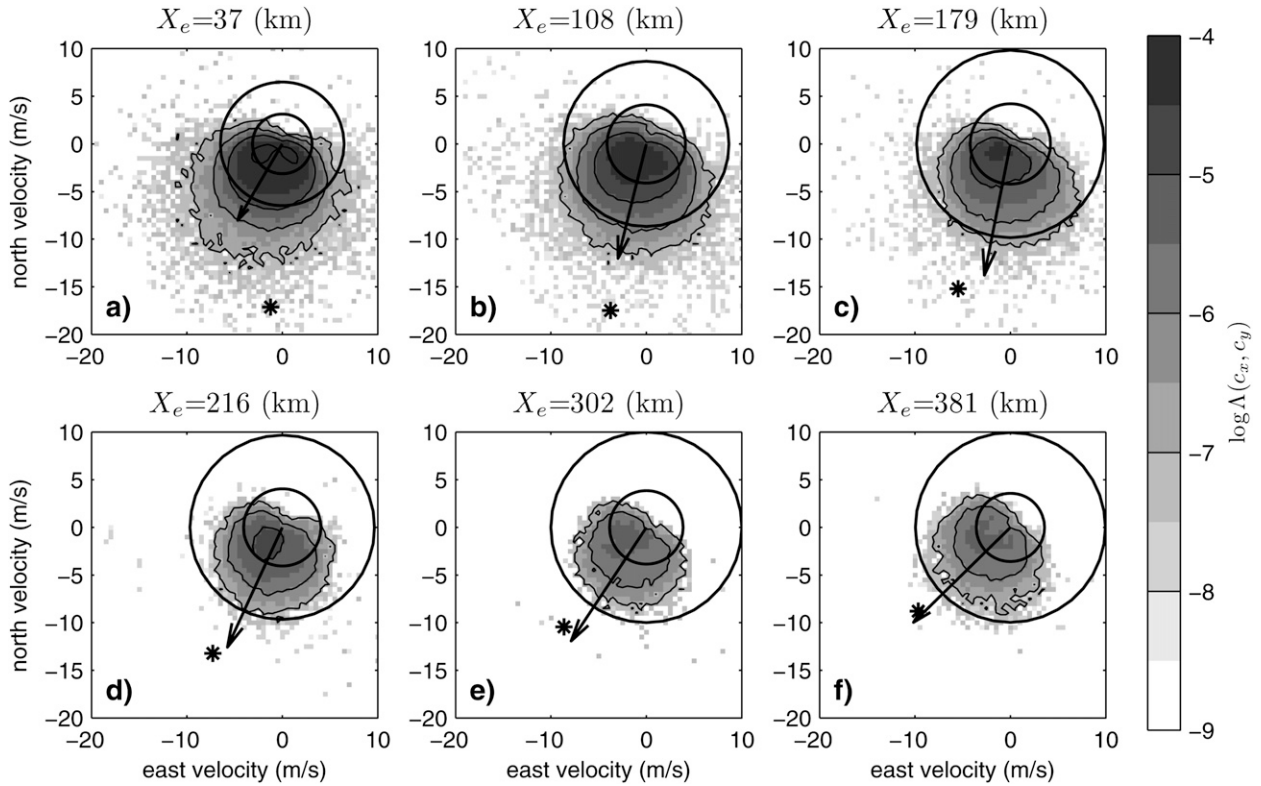


FIG. 5. Example directional breaking distributions $\Lambda(\mathbf{c})$ for six image sequences as the aircraft moved offshore during RF 10. Note that the shading is logarithmic. The effective fetch at each estimate is listed above each panel. The concentric solid black circles indicate the extent of the estimated equilibrium range, $c_T < c < 0.7c_p$, where c_T is the phase speed at which the omnidirectional spectra transitions from a -2.5 to a -3 power law. The black arrows show the dominant wave direction and terminate at the spectral peak phase speed. The asterisks show the 10-m wind direction and magnitude. The wave age c_p/u_{sp} of these six estimates is 16, 17, 21, 23, 26, and 31 as fetch increases.

Gemrich et al. (2008) present directional distributions of $\Lambda(c, \theta)$ that appear to be in agreement with the GOTEX directional distributions for the faster speeds ($c > 3 \text{ m s}^{-1}$). They observe breaking for all downwind directions, and the weighted spreading width

$$\left[\frac{\int_{-\pi}^{\pi} \theta^2 \Lambda(c/c_p, \theta) d\theta}{\int_{-\pi}^{\pi} \theta^2 \Lambda(c/c_p, \theta) d\theta} \right]^{1/2}$$

is about 30° , independent of wave scale. The GOTEX weighted spreading width varies from nearly 40° for small-scale waves to 20° at the larger scales. For the youngest seas, the weighted spreading width is consistent with the directional spreading of the wave field. However, as the seas approach full development, the directional distribution of $\Lambda(c, \theta)$ becomes more narrow. The directional distributions presented by Melville and Matusov (2002) show more breaking in the upwind direction than the GOTEX observations.

One measure of the directional distribution of $\Lambda(\mathbf{c})$ is the integral of $\Lambda(c, \theta)$ with respect to c , normalized by the total length of wave breaking:

$$\hat{\Lambda}(\theta) = \frac{\int_0^\infty \Lambda(c, \theta) c dc}{\int_{-\pi}^{\pi} \int_0^\infty \Lambda(c, \theta) c dc d\theta}. \tag{13}$$

This yields a probability distribution of breaking as a function of the direction of breaking. The distributions of $\hat{\Lambda}(\theta)$ are shown in the top row of Fig. 6. In Fig. 6a', $\theta_w = 0$ is the local mean wind direction. The values $\theta_w = \pm\pi/2$ are indicated with dashed lines in Fig. 6a' because one of the criteria of active breaking involves the breaking direction and unit normal less than $\pi/2$ from the wind direction are more likely to be actively breaking. The classification simply acts as a switch, not as a function of the angle θ_w , so the directional distribution for $|\theta_w| < \pi/2$ is not affected by this criterion. Phillips (1985) gives the directional distribution of $\Lambda(\mathbf{c})$ as a function like $\cos^{3p}\theta_w$, with p in the range $0.5 < p < 2$. When normalized consistently, with $-\pi/2 < \theta < \pi/2$, our data show the closest agreement with $p = 0.5$, with our observations being somewhat wider than the $\cos^{3p}\theta$ function, as shown in black in Fig. 6a'.

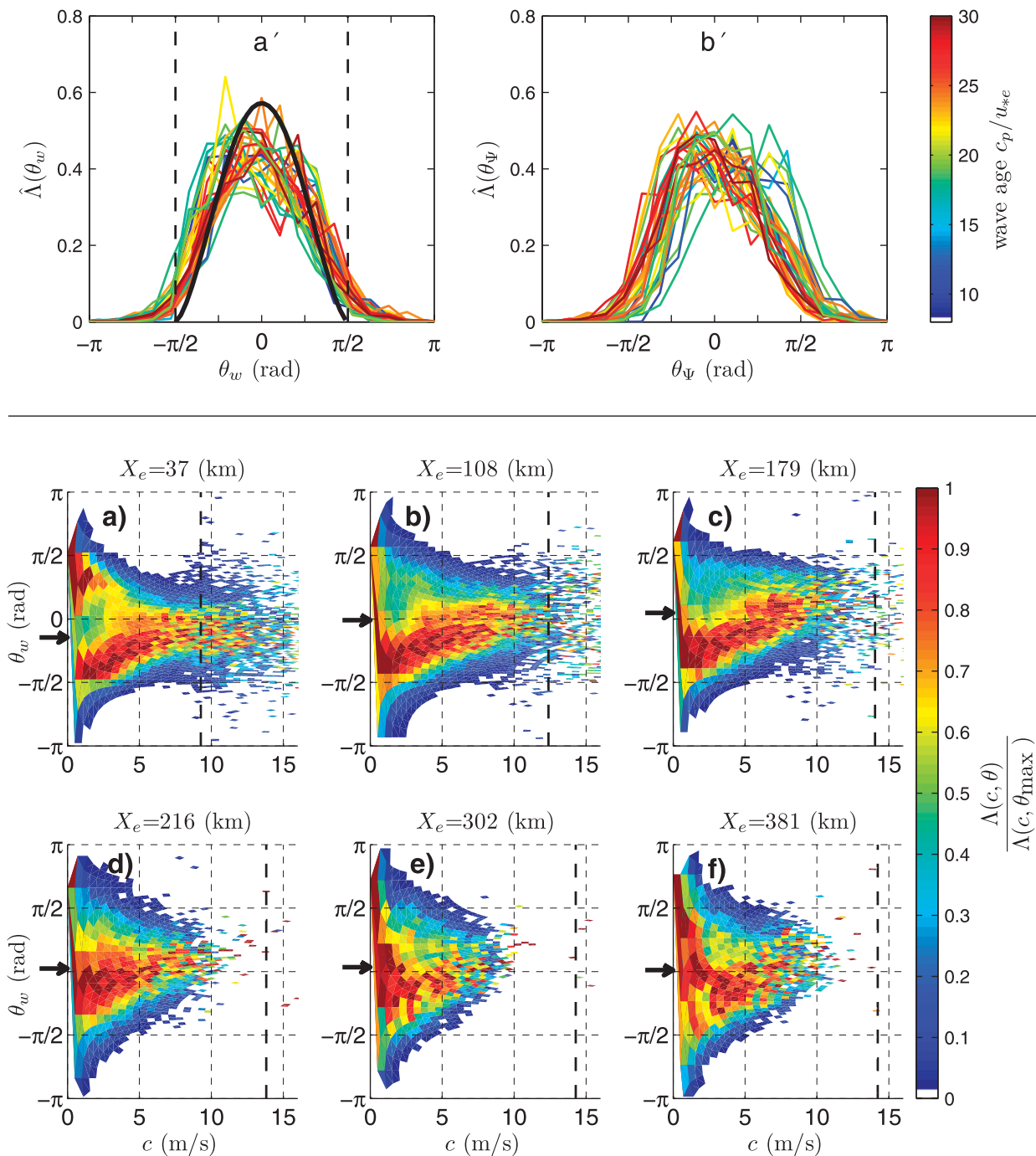


FIG. 6. (a'),(b') The normalized directional distribution of breaking [Eq. (13)], with color corresponding to wave age c_p/u_{*e} : (a') θ_w is the direction of breaking relative to the mean wind direction and (b') θ_Ψ is the direction of breaking relative to the dominant wave direction. The vertical dashed lines in (a') indicate values of $-\pi/2$ and $\pi/2$, which are used in the determination of active breaking fronts in the algorithm. Breaking with $|\theta_w| > \pi/2$ is suppressed in the processing. Black curve shows $\cos^{3p}\theta_w$, with $p = 0.5$ for the $\Lambda(c, \theta_w)$ distributions in (a)–(f) six sample image sequences. The effective fetch is indicated above each panel. Vertical dashed lines indicate the spectral peak phase speed, and arrows along the y axis indicate the dominant wave direction. $\Lambda(c, \theta_w)$ has been normalized by the maximum of $\Lambda(c, \theta_w)$ for each value of c .

It should be noted that the $\hat{\Lambda}(\theta)$ distribution changes with the interpretation of the speed of breaking. The present data are computed with the elemental method in which the velocity is a function of both space and time and is normal to the breaking crest. Consideration of the full translational, rather than the normal, velocity results in a more narrow directional distribution, in closer agreement with $p = 1$. Consideration of a single breaking velocity as a function of time narrows the distribution further to $p = 1$ or 2, and consideration of a single breaking velocity for each breaking event results in narrow directional distributions roughly consistent with $p = 3$. We maintain that the elemental method is the preferred interpretation of breaking speeds and lengths on the sea surface. This directly affects the comparison between observations and the Phillips (1985) discussion about the appropriate values of p in his formulation.

In Fig. 6b', $\theta_{\Psi} = 0$ is the local dominant wave direction. The directional distributions show better agreement with the wind direction (Fig. 6a') than with the local dominant wave direction (Fig. 6b'). In many cases, the wind direction is aligned with the dominant wave direction (Fig. 5). In all cases, the mean breaking direction $\bar{\theta}_{\Lambda}$ agrees with the wind direction to within 20° , where the mean breaking direction is defined as

$$\bar{c}_x = \frac{\iint c_x \Lambda(c_x, c_y) dc_x dc_y}{\iint \Lambda(c_x, c_y) dc_x dc_y};$$

$$\bar{c}_y = \frac{\iint c_y \Lambda(c_x, c_y) dc_x dc_y}{\iint \Lambda(c_x, c_y) dc_x dc_y};$$

$$\bar{\theta}_{\Lambda} = \tan^{-1}\left(\frac{\bar{c}_y}{\bar{c}_x}\right).$$

The $\hat{\Lambda}(\theta)$ distributions in the top row of Fig. 6 show that a small fraction of breakers are traveling opposite to the wind ($|\theta_w| > \pi/2$) or opposite to the dominant wave direction ($|\theta_{\Psi}| > \pi/2$). It is of interest to know what scale of wave is contributing to the tails of the distributions. In Figs. 6a–f, $\Lambda(c)$ is shown in polar coordinates. The original data are determined with a resolution $\Delta c = 0.5 \text{ m s}^{-1}$, and this resolution is retained in the polar representation without smoothing or resampling the data on a regular (c, θ_w) grid. The data are normalized by $\Lambda(c, \theta_{\max})$, where θ_{\max} is the direction of maximum breaking for each value of c . This facilitates visualization of the peak breaking direction as a function of breaking speed c . The vertical dashed line in each panel indicates the local spectral peak phase speed, and the arrows along the ordinate indicate the dominant wave direction. It is apparent that the slower breaking facets have a wider

directional distribution, whereas the faster breaking facets tend to be aligned within 90° of the wind direction. In particular, the lateral expansion of the breaking crest, which occurs at angles away from the wind direction, contributes to the wide directional distribution at slow speeds.

Recent field data (Hwang and Wang 2001; Romero and Melville 2010a) show that wave spectra directional distributions exhibit a bimodal structure rather than a unimodal distribution such as $\cos^p \theta$. The bimodality is also evident in the wave slope spectrum, and breaking strength is thought to be related to the wave slope. Although Figs. 6a', b' show that the total breaking directional distribution is unimodal and aligned with the wind direction, Fig. 6a shows a clear bimodality in the directional distribution of $\Lambda(c, \theta_w)$ for slow speeds, $c < 3 \text{ m s}^{-1}$. This type of bimodality is observed in 75% of the $\Lambda(c, \theta)$ observations with the fetch under 50 km. Figures 6b, c show an asymmetry in the breaking direction for $c < 5 \text{ m s}^{-1}$. In general, the asymmetry favors the branch closer to the wind direction when the asymmetry occurs for the faster breaking speeds ($c > 5 \text{ m s}^{-1}$), and the dominant wave direction differs from the wind direction by more than 6° . The bimodal directional distribution is apparent when $\Lambda(c)$ is computed using elemental speeds, with velocity normal to the breaking crest.

d. Comparison of $\Lambda(c)$ to breaking rate and whitecap coverage

The total length of breaking per unit sea surface area, $\int \Lambda(c) dc$, as well as the first two moments of $\Lambda(c)$ shows a strong correlation with the observed whitecap coverage and breaking rate (Fig. 7). The n th moment of $\Lambda(c)$ is defined as

$$\int_0^\infty c^n \Lambda(c) dc. \tag{14}$$

The first moment of $\Lambda(c)$ is equal to the fraction of the sea surface that is turned over per unit time, equivalent to the passage rate of breakers past a fixed point (Phillips 1985). A straightforward estimate of the total breaking rate from the GOTEX data is the fraction of points on the image that pass from below to above the brightness threshold. However, Kleiss and Melville (2010) found that this method overestimated the breaking rate because of the motion of large, bright patches of old foam. The old foam motion may be due to surface currents or advection by orbital motion. To obtain an estimate of the breaking rate due solely to active breaking, we define the active breaking rate as connected regions of the image that pass from below to above the brightness threshold by a white area that contains at least one actively breaking point identified in the $\Lambda(c)$ processing.

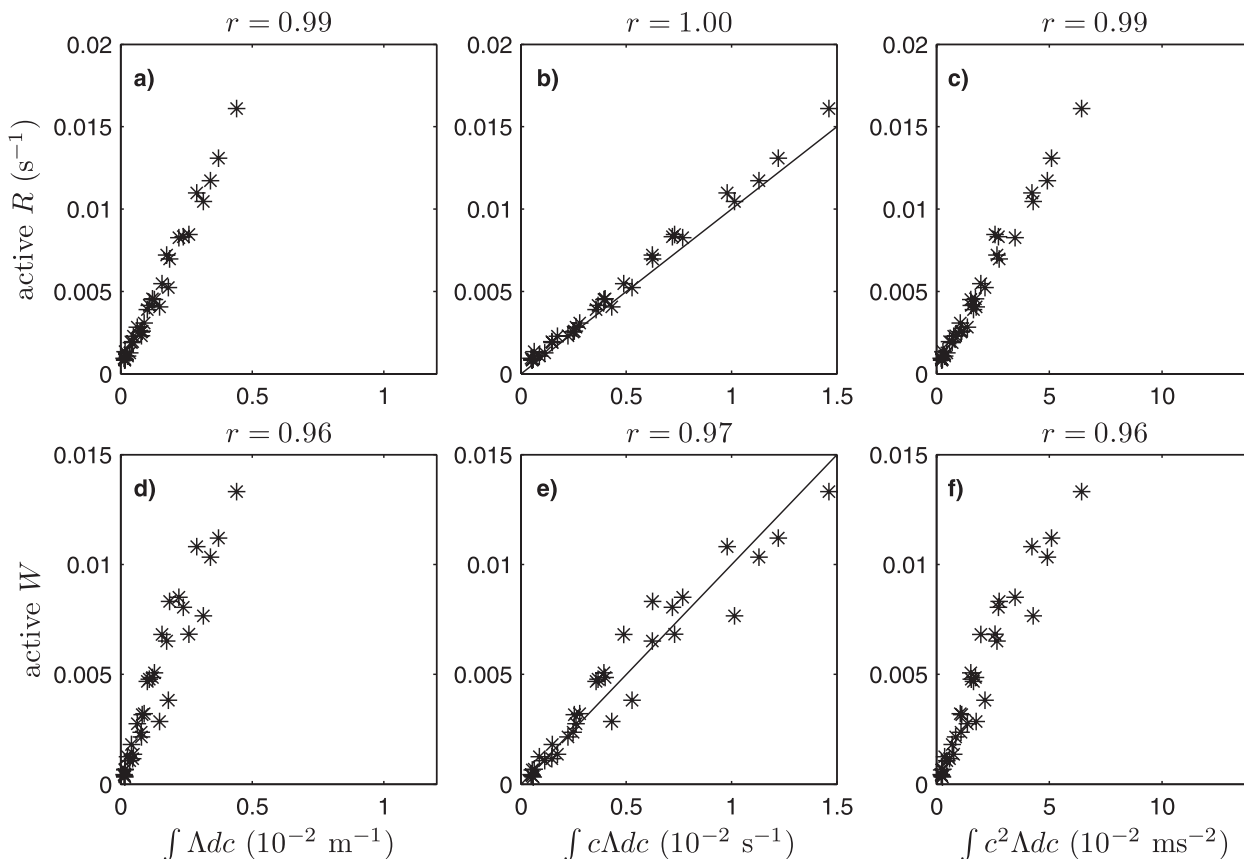


FIG. 7. Comparison of the moments of $\Lambda(c)$ to (a)–(c) the active breaking rate and (d)–(f) the active whitecap coverage. The moments of $\Lambda(c)$ are indicated at the bottom of the figure. The correlation coefficient r is shown above each panel, and one-to-one lines are shown in (b) and (e).

This calculation of the active breaking rate is not independent of the $\Lambda(c)$ processing. It does not test the ability of the $\Lambda(c)$ processing to identify breaking events. However, agreement of the active breaking rate to the first moment of $\Lambda(c)$ suggests that, on average, the full length and the appropriate speed of breaking, as constrained by any initial thresholding, is captured.

Jessup and Phadnis (2005), Gemmrich et al. (2008), and Thomson and Jessup (2009) compared independent estimates of the breaking rate to the first moment of their $\Lambda(c)$ observations. Although such a test is useful, it should be approached with caution, as Kleiss and Melville (2010) showed that even a grossly incorrect $\Lambda(c)$ distribution showed a near-perfect agreement with the breaking rate so long as consistent thresholds identifying breaking were used for both.

The active breaking rate is shown versus the integral of $\Lambda(c)$ and the first two moments in Figs. 7a–c, with a one-to-one line superimposed on Figs. 7b,e. Each moment of $\Lambda(c)$ shows a strong correlation with the active breaking rate, as shown above each panel.

The total whitecap coverage is the fraction of the image covered with visible bubble patches. We can also

consider the active whitecap fraction as the fraction of the image covered with bubble patches associated with actively breaking waves. Again, we use the $\Lambda(c)$ results to distinguish between active and residual foam patches. A foam patch that is tracked for N consecutive images may be found to be actively breaking for zero to N of those images. For our analysis, we only consider those breaking events that are actively breaking for at least five observations, or 0.2667 s.

Figures 7d–f show strong correlations between the zeroth to second moment of $\Lambda(c)$ and the active whitecap coverage. If the bubbles generated by breaking persist for a time τ_p on the surface, then Phillips (1985) proposed that the whitecap coverage is

$$W = \int c\tau_p \Lambda(c) dc. \quad (15)$$

Likewise, the active whitecap coverage is

$$W_A = 0.5 \int c\tau \Lambda(c) dc, \quad (16)$$

where τ is the duration of active breaking. The factor of 0.5 arises from the fact that the observation may occur at

any time during active breaking, assuming a uniform growth rate of the breaker area (Kleiss 2009, appendix B). We are primarily concerned with actively breaking waves, so we focus our attention on Eq. (16). If the duration of breaking, τ , is a constant, then the active whitecap coverage would be proportional to the first moment of $\Lambda(c)$ (Eifler 2005; Myrhaug and Holmedal 2008). However, Froude scaling suggests that the duration of breaking is proportional to the period of the wave that is breaking, $\tau \propto T$, and $T = 2\pi c_l/g$ from the deep water dispersion relation, where c_l is the intrinsic phase speed of the wave that is breaking. As discussed in Kleiss and Melville (2010), the observed breaking speed c may be related to the underlying phase speed after correction for underlying long wave orbital velocities and surface drift current. This implies that the active whitecap coverage would be proportional to the second moment of $\Lambda(c)$ (Reul and Chapron 2003). Such Froude scaling has been observed in field (Thorpe and Hall 1983) and in numerical experiments (Kennedy and Snyder 1983).

Figures 7e,f show an equally good agreement of W_A with the first and second moments of $\Lambda(c)$, indicating that comparison of the moments of $\Lambda(c)$ to the active whitecap coverage is not sufficient to distinguish between a constant breaking duration τ or a scale-dependent breaking duration $\tau \propto c_l$ from our data. The one-to-one comparison of W_A with the first moment indicates that the mean duration of breaking is 2 s, from Eq. (16). Note that this time scale does not reflect the actual observed duration of breaking, which is limited by the residence time in our images, but reflects the mean ensemble aspect ratio of the breaking crest length to the width of the foam patch. In other words, the mean ensemble duration is estimated from knowledge of the breaking speed, breaking crest length, and foam patch area. In Eq. (16) the foam patch area is represented by W_A , the breaking crest length is represented by Λ , and the foam patch width is given by $c\tau$ when the motion and degassing at the rear edge of the foam patch is neglected.

Note that Eqs. (15) and (16) both have an implicit assumption that, once breaking has occurred at a given location, that location remains in the foam patch for the bubble residence time τ_p . In fact, it appears that, during the early stages of breaking, the breaking passes by a point and the bubbles do not remain at that point but are carried forward with the breaking wave crest. In other words, the rear of the bubble patch is not stationary to leading order when a wave is beginning to break. During the later stage of breaking, the rear of the foam patch does appear to remain more stationary. The model relating the whitecap coverage to $\Lambda(c)$ could be improved by including this effect.

The equally good agreement of the two moments may be due to the shape of the $\Lambda(c)$ distributions (Fig. 2) that have a relatively narrow peak, such that differences between adjacent moments, say, n and $n + 1$, are small and dominated by the peak in $\Lambda(c)$.

e. Whitecap coverage: Wind speed dependence

The GOTEX dataset did not easily lend itself to a single brightness threshold capable of capturing both the active W_A and residual W_B whitecap coverage, including all old foam and streaks. Previous studies (Bondur and Sharkov 1982; Monahan et al. 1985; Monahan and Woolf 1989) have found that the residual foam coverage W_B is about 10 times the active whitecap coverage W_A . These studies determined the foam patch extent manually. From our experience, a single brightness threshold criterion compares well with manual identification of bright, actively breaking waves but may not capture the full extent of dim old foam and foam streaks.²

We define the active whitecap coverage W_A as the fraction of the sea surface covered with foam patches that have some fraction of their perimeter actively breaking for at least $2/3$ s. This minimum duration was implemented for consistency across different methods of calculating $\Lambda(c)$ (see Kleiss and Melville 2010) and aims to discriminate against old foam patches that may have a small number of falsely identified actively breaking segments. The thresholded whitecap coverage W_T is simply the fraction of the image covered with foam patches brighter than a brightness threshold. The mean ratio of W_T to W_A is 1.5, which is much less than the previously observed ratios of W_B/W_A of about 10. An analysis beyond that of a single brightness threshold is needed to obtain the total whitecap coverage W_B from the GOTEX dataset. We deliberately use the term “thresholded whitecap coverage” rather than “total whitecap coverage” to emphasize that our method of thresholding does not capture the full extent of residual foam coverage W_B , defined to include all old foam patches and streaks.

In Fig. 8, the GOTEX whitecap coverage data are plotted against wind speed and friction velocity and compared to previous studies of active whitecap coverage versus winds. The GOTEX data are shown by solid circles colored by the wave age, and lines show regressions through previous studies. The thresholded whitecap coverage W_T in Figs. 8a and 8c includes images from research flights 2, 5, 7, 9, and 10 with aircraft altitude ranging from 30 to 1600 m and 10-m wind speed from

² Bondur and Sharkov (1982) obtained images from an aircraft, and the Monahan studies obtained images from a ship-mounted camera. The oblique view from ship-mounted cameras may also affect the results.

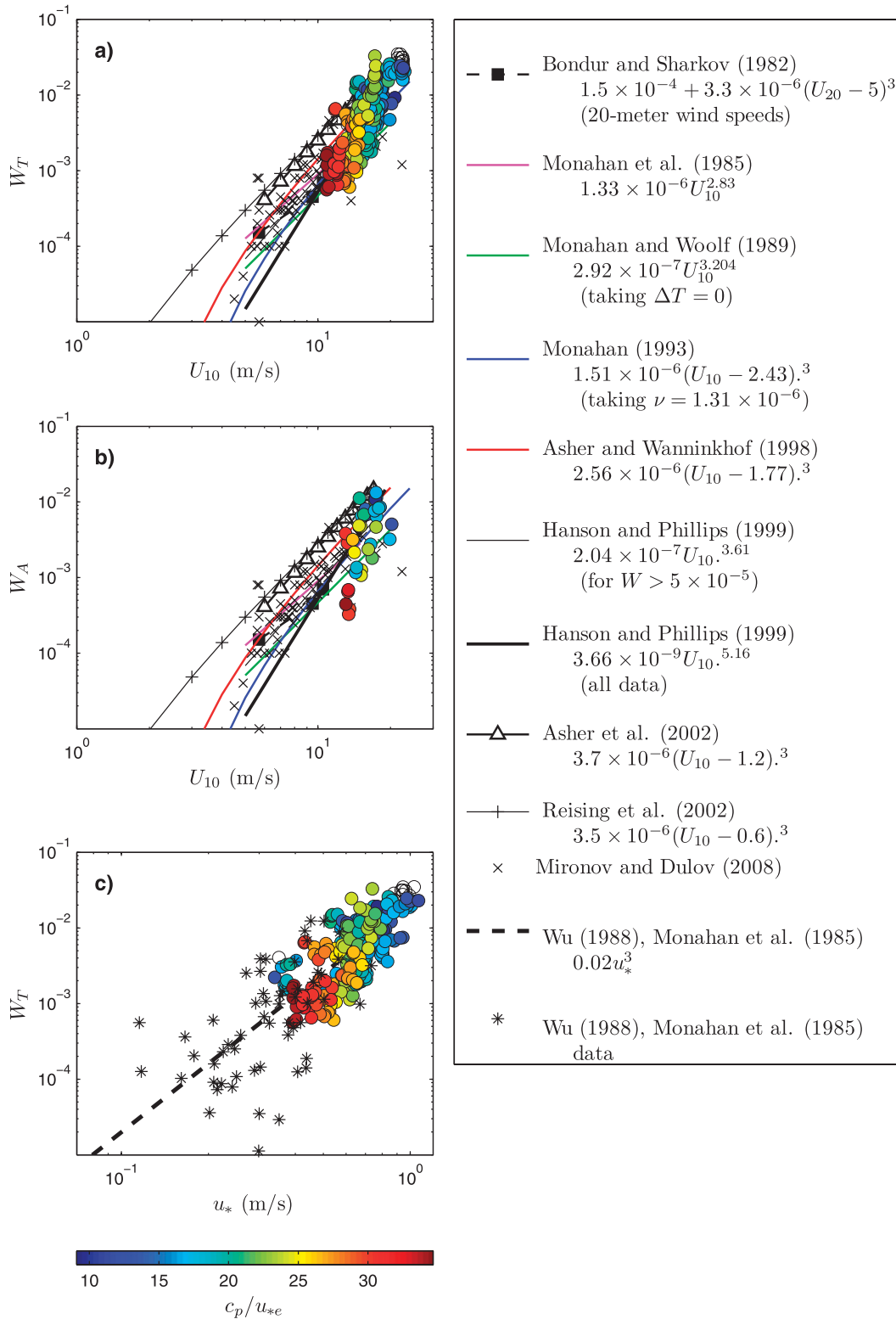


FIG. 8. Comparison of the GOTEX whitecap coverage to previous studies of active whitecap coverage W_A vs wind speed. The GOTEX data are shown by circles with color corresponding to effective wave age c_p/u_{*e} . Open symbols do not have an estimate of c_p . (a) GOTEX thresholded whitecap coverage W_T vs 10-m wind speed and (b) GOTEX strictly active whitecap coverage W_A vs 10-m wind speed. Previously published studies are given by the equations and notes on the right. (c) GOTEX thresholded whitecap coverage vs friction velocity u_* , with data (asterisks) and the regression (dashed line) from the Wu (1988) reanalysis of Monahan et al. (1985).

10 to 23 m s⁻¹. The strictly active whitecap coverage W_A in Fig. 8b is limited to image sequences that underwent kinematic processing, all from roughly 400-m altitude, reducing the number of observations. Each colored circle in the figure represents the average whitecap coverage of sequential images that cover roughly 3 km² of nonoverlapping sea surface area. The color indicates the effective wave age c_p/u_{*e} . The wind and wave data have been spatially interpolated from the locations of radome wind and scanning lidar wave measurements, respectively (see section 2).

A number of previous studies reporting active whitecap coverage are also shown. The studies after 1990, except for Mironov and Dulov (2008), used a single threshold to determine active whitecap coverage.³ Monahan (1993) reported a relationship for W_A dependent upon the kinematic viscosity of water ν :

$$W_A = 1.98 \times 10^{-12} \nu^{-1} (U_{10} - 2.2 \times 10^{-2} \nu^{1/3})^3. \quad (17)$$

Monahan references a water temperature of 11.1°C in his paper, so the viscosity of water is taken to be 1.31×10^{-6} m² s⁻¹ to obtain the line shown in Figs. 8a and 8b. Asher and Wanninkhof (1998), Hanson and Phillips (1999), Asher et al. (2002), and Reising et al. (2002) all follow the methodology put forth in Monahan (1993) for determination of the whitecap coverage fraction from sea surface images. Hanson and Phillips (1999) report two relationships of W to 10-m wind speed, one for all data and one in which they discard data with $W < 5 \times 10^{-5}$. All of the studies in Fig. 8 except for Bondur and Sharkov (1982) are from cameras mounted on a research vessel, platform, or tower, observing the ocean from oblique angles. Images captured at oblique angles impart serious distortions of the sea surface.

Although power-law relationships of whitecap coverage with wind speed and friction velocity are dimensionally inhomogeneous, they are widely reported in the literature and are presented here for comparison with previous studies. In Fig. 8a, the GOTEX data generally fall within the range of previous studies of active whitecap coverage but show a steeper increase of whitecap coverage with increasing wind speed. This family of results is roughly a factor of 10 lower than published studies of total whitecap coverage W_B (not shown). A linear regression through the GOTEX data in logarithmic coordinates results in the relationship

$$W_T = 6.58 \times 10^{-9} U_{10}^{4.9}; \quad r = 0.83, \quad (18)$$

where r is the correlation coefficient. This exponent compares well with the relationship from Hanson and Phillips (1999), $W_A = 3.66 \times 10^{-9} U_{10}^{5.16}$.

Monahan (1993) suggested the relationship $W^{1/3} = a_1(U - a_2)$, where a_1 and a_2 are constants. Least squares linear regression in this form results in

$$W_T = 5.83 \times 10^{-6} (U_{10} - 5.9)^3; \quad r = 0.84. \quad (19)$$

Expressions of the form $W^{1/3} = a_1(U_{10} - a_2)$ generally suggest that a_2 is related to the wind speed at which whitecaps first begin to appear on the ocean surface, with previous studies giving a_2 in the range of 0.6–2.43. The GOTEX result of $a_2 = 5.9$ is consistent with the steeper power-law dependence. Expressions (18) and (19) appear nearly identical over the range $10 < U_{10} < 23$ m s⁻¹; the mean absolute difference is 6×10^{-4} . The wind speed dependence will be further addressed in the discussion.

In Fig. 8b, the strictly active whitecap coverage W_A from GOTEX is compared to published studies. The bulk of the data falls among the previous studies, with a notable exception of four GOTEX data sequences that have 10-m wind speeds of 13–14 m s⁻¹ and whitecap coverage less than 0.001. These four data points represent image sequences captured farthest from the coast on the late morning of research flight 10. Manual inspection of the images indicates that the choice of brightness threshold is accurate and the images are of high quality. There is simply not much wave breaking. Observing less than 0.1% active whitecap coverage at wind speeds of 13–14 m s⁻¹ is most reasonably a result of the well-developed sea state and the decreasing wind with fetch.

Linear regressions through the strictly active whitecap coverage are

$$W_A = 3.51 \times 10^{-10} U_{10}^{5.84}; \quad r = 0.60 \quad (20)$$

and

$$W_A = 4.34 \times 10^{-6} (U_{10} - 6.02)^3; \quad r = 0.55. \frac{x - \mu}{\sigma}. \quad (21)$$

In the GOTEX, u_* is the primary observed wind variable, measured by the fluctuations of the turbulent wind and computed using the Reynolds stresses (Romero and Melville 2010a). Wu (1979) proposed that the whitecap coverage should be proportional to u_*^3 , based on dynamical arguments. There are a number of studies that report whitecap coverage and wind stress (Wu 1988; Zhao and Toba 2001; Stramska and Petelski 2003; Lafon et al. 2004, 2007; Sugihara et al. 2007). However, the only relationship of active whitecap coverage W_A to u_* among these studies is from the Wu (1988) reanalysis of the Monahan et al. (1985) data, resulting in $W_A = 0.02u_*^3$.

³ This is actually identical to what we are calling the thresholded whitecap coverage W_T and highlights the confusion of nomenclature in this area.

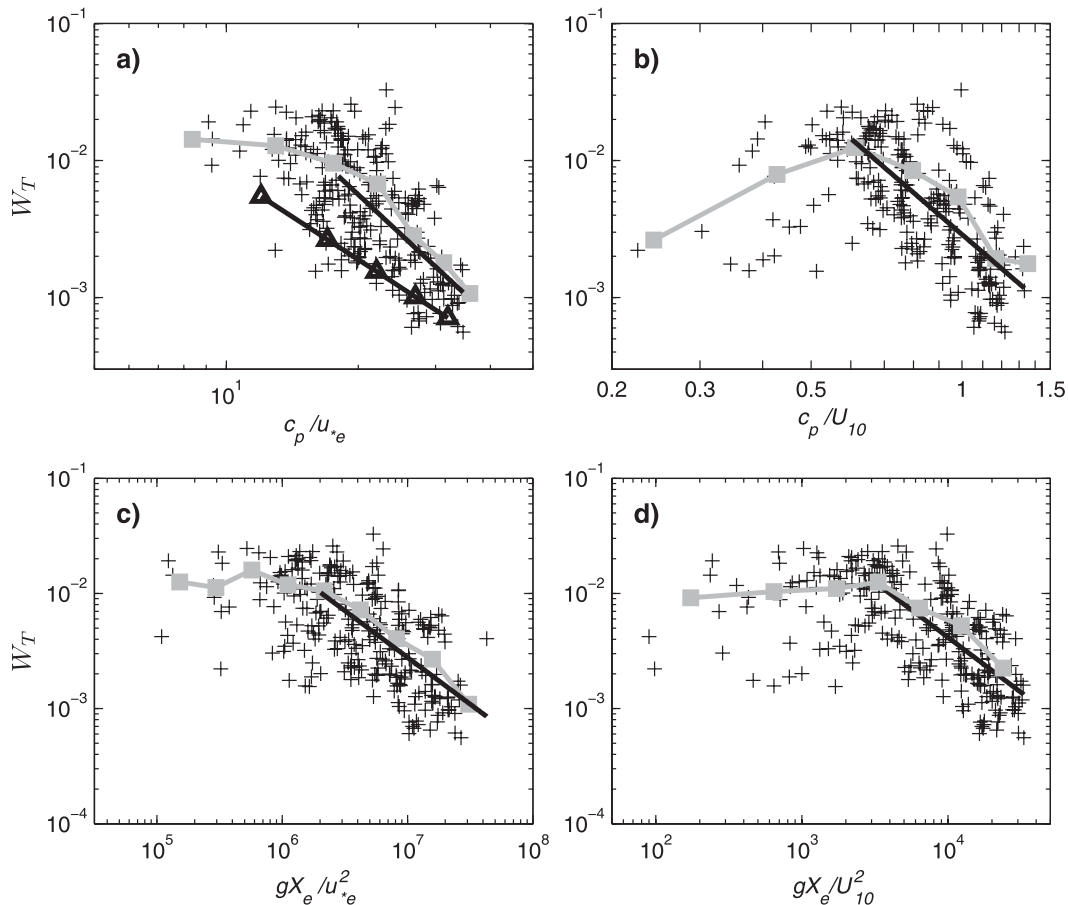


FIG. 9. Thresholded whitecap coverage W_T vs wave age (a) c_p/u_{*e} and (b) c_p/U_{10} and vs nondimensional fetch (c) gX_e/u_{*e}^2 and (d) gX_e/U_{10}^2 . The GOTEX data from all aircraft altitudes, covering 3 km² sea surface area, are shown by black crosses. The gray line with squares in each panel shows the bin average of the data. The black lines in (a)–(d) show Eqs. (23), (25), (26), and (27), respectively. The line with triangles in (a) shows Kraan et al. (1996) [Eq. (24)].

Figure 8c shows the whitecap coverage, as obtained from a threshold analysis on all processed images, versus the friction velocity. A least squares linear regression of the data in logarithmic coordinates yields the relationship

$$W_T = 0.02u_{*e}^{3.1}; \quad r = 0.73. \quad (22)$$

The coefficient that satisfies $W_T = au_*^3$ in a least squares sense is $a = 0.025$. The data from Monahan et al. (1985) with friction velocity as given in Wu (1988) is shown by black asterisks for comparison.

The thresholded whitecap coverage is related to the effective friction velocity u_{*e} ,

$$W_T = 0.02u_{*e}^{2.6}; \quad r = 0.63$$

for all data at all altitudes and

$$W_T = 0.02u_{*e}^{3.1}; \quad r = 0.76$$

for images captured at altitudes less than 500 m.

f. Whitecap coverage: Wave age dependence

The dependence of GOTEX observed whitecap coverage versus wave age and dimensionless fetch is shown in Fig. 9. We present the thresholded whitecap coverage W_T because of the larger number of observations and the close relationship of $W_T \approx 1.5W_A$, which is well within the scatter of the data. Consistent with Lafon et al. (2004, 2007), our data show that the whitecap coverage decreases with wave age for wave ages greater than about 15. For smaller wave ages, there is no apparent trend. The linear fit in logarithmic coordinates for the GOTEX data with $c_p/u_{*e} > 15$ is

$$W_T = 18 \left(\frac{c_p}{u_{*e}} \right)^{-2.71}; \quad r = 0.62. \quad (23)$$

If we restrict the region to $c_p/u_{*e} > 20$, the power law exponent is -3.41 . The bin averages of the data are shown by the gray line with squares. Kraan et al. (1996) also

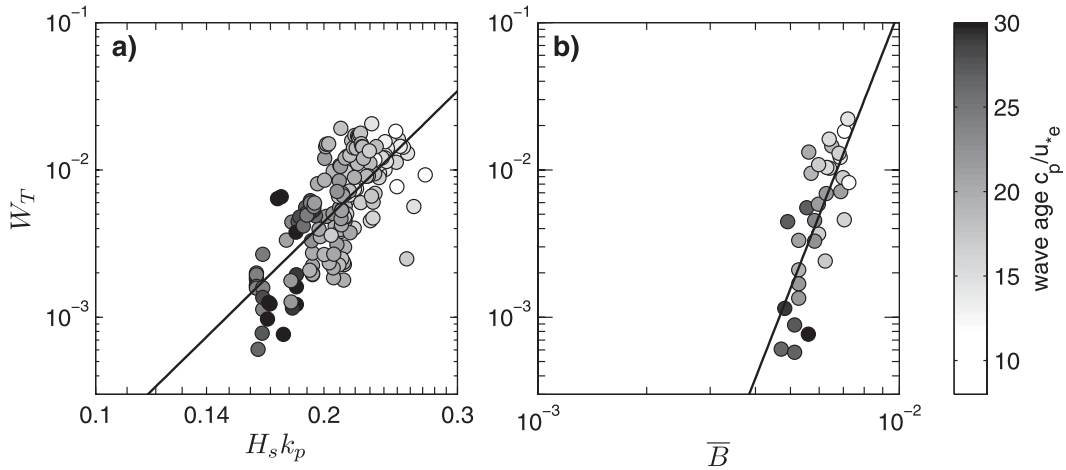


FIG. 10. Total thresholded whitecap coverage W_T vs measures of wave steepness: (a) significant slope $H_s k_p$ and (b) the mean saturation over the range $1 < k/k_p < 25$ [Eq. (29)]. The GOTEX data are given by shaded circles. The black lines are least squares fits to the data in logarithmic coordinates [Eqs. (28) and (30)].

report active whitecap coverage as a function of wave age and their result,

$$W_A = 0.96 \left(\frac{c_p}{u_{*e}} \right)^{-2.08}, \quad (24)$$

is shown by the line with triangles.

Wave age can also be expressed as c_p/U_{10} , and its relationship to whitecap coverage is shown in Fig. 9b for completeness. A power law fit for $c_p/U_{10} > 0.6$ is given by the solid line,

$$W_T = 2.98 \times 10^{-3} \left(\frac{c_p}{U_{10}} \right)^{-3.15}; \quad r = 0.68. \quad (25)$$

Again, the gray line with squares is the bin average of the data. Our results agree with those of Lafon et al. (2007), showing an initial increase in whitecap coverage with wave age, with a maximum around $(c_p/U_{10}) = 0.6$, followed by a decrease.

The relationship between the total whitecap coverage and the dimensionless fetch is shown in Figs. 9c,d. The linear regression in logarithmic coordinates is shown by the black line,

$$W_T = 1.34 \times 10^3 \left(\frac{gX_e}{u_{*e}^2} \right)^{-0.81}; \quad r = 0.59 \quad (26)$$

for dimensionless fetch $(gX_e u_{*e}^{-2})$ greater than 2×10^6 and

$$W_T = 27.8 \left(\frac{gX_e}{U_{10}^2} \right)^{-0.96}; \quad r = 0.66 \quad (27)$$

for dimensionless fetch $(gX_e U_{10}^{-2})$ greater than 3000. The gray line with squares in each panel indicates the bin average of the data. This result depicts a consistent relationship of wave breaking with wave age as that shown in Fig. 2h. This consistency is suggested from the close relationship of the integrated moments of $\Lambda(c)$ and the active whitecap coverage (Figs. 7d,f).

g. Whitecap coverage: Slope dependence

Laboratory experiments (Melville and Rapp 1985; Rapp and Melville 1990; Melville 1994; Banner and Peirson 2007; Drazen et al. 2008) have examined the relationship between the wave slope and the strength of breaking. For the purposes of comparison with whitecap coverage, a mean estimate of the slope of the wave field is desired. One measure of steepness is the significant slope $H_s k_p$, where H_s is the significant wave height $4(\int \Psi(\mathbf{k}) d\mathbf{k})^{1/2}$, $\Psi(\mathbf{k})$ is the wave height spectrum, and k_p is the spectral peak wavenumber. The whitecap coverage data as a function of the significant slope is shown in Fig. 10a. The linear least squares regression through the data, in logarithmic coordinates, yields the relationship

$$W_T = 14.8(H_s k_p)^{5.0}; \quad r = 0.73, \quad (28)$$

where r is the correlation coefficient. Another measure of the wave steepness is the saturation, a dimensionless variable defined as

$$B(k) = \int_0^{2\pi} k^4 \Psi(k, \theta) d\theta. \quad (29)$$

The saturation is related to the spectral mean square slope (Phillips 1977; Hwang and Wang 2001; Banner

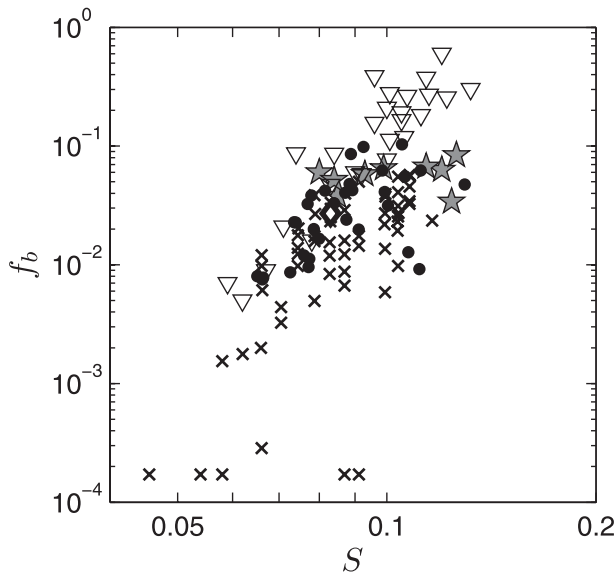


FIG. 11. The breaking rate normalized by the dominant wave period vs the spectral peak steepness S [Eq. (31)]. The symbols are crosses: Katsaros and Ataktürk (1992), gray stars: Banner et al. (2000) Black Sea data, diamonds: Banner et al. (2000) Southern Ocean data, triangles: Babanin et al. (2001) Lake George data, and black circles: GOTEX data.

et al. 2002). For our data, the omnidirectional spectra are computed from the ATM sea surface measurements. Each spectrum is fit to a -2.5 power law over the interval $2k_p < k < 0.35 \text{ rad m}^{-1}$, where the upper limit is set by the noise floor of the ATM. This fit is extended until it intersects the saturation range, at a level $\phi(k) = 7 \times 10^{-3} k^{-3}$, which then describes the spectra for the higher wavenumbers. The transition wavenumber k_T between the $k^{-2.5}$ and k^{-3} power-law behaviors range from $5k_p$ to $25k_p$ (see Romero and Melville 2010a,b; Fig. 6). The mean of the saturation \bar{B} is taken over the range $1 < k/k_p < 25$.

In Fig. 10b, the whitecap coverage is compared to the mean saturation \bar{B} . Owing to the sensitivity of the calculation of B on the wave spectra, only those image files that directly overlap with wave spectra estimates are shown. A linear fit to the data in logarithmic coordinates yields the relationship

$$W_T = 1.25 \times 10^{11} \bar{B}^{6.0}; \quad r = 0.76, \quad (30)$$

shown with the black line in Fig. 10b.

Another common estimate of the amount of breaking on the ocean surface is the breaking rate R . The breaking rate normalized by the period of the dominant waves, $f_b = RT_p$, has been reported by many authors (Thorpe and Humphries 1980; Longuet-Higgins and Smith 1983; Holthuijsen and Herbers 1986; Katsaros and Ataktürk 1992; Thorpe 1992; Gemmrich and Farmer 1999; Xu et al.

2000; Banner et al. 2000; Babanin et al. 2001; Gemmrich et al. 2008). Thorpe (1993) found that the normalized breaking rate appeared to increase with wave age, but later studies (Gemmrich and Farmer 1999; Banner et al. 2000) found that neither wave age, wind speed, nor wind stress collapsed diverse datasets well. Banner et al. (2000) proposed the spectral peak steepness,

$$S = \frac{H_p k_p}{2}, \quad (31)$$

where

$$H_p = 4 \left(\int_{0.5k_p}^{1.7k_p} \phi(k) dk \right)^{1/2}.$$

Banner et al. (2000) assert that S reflects the mean steepness of the dominant waves and also provides a measure of their nonlinearity, as well as the nonlinear energy flux within dominant wave groups.

The normalized breaking rate did not collapse well with wave age nor wind speed when compared to previous studies but showed a favorable comparison when plotted against S , as shown in Fig. 11. Banner et al. (2000) and Babanin et al. (2001) also present factors to account for the surface shear, wind forcing strength, and finite depth, which we do not incorporate here. As in Fig. 7, the active breaking rate is shown in Fig. 11.

5. Discussion

a. Whitecap coverage related to wind speed

Figure 8 showed that the GOTEX dataset had a stronger dependence on wind speed than many previous studies comparing whitecap coverage to wind speed. The steep trend of the whitecap coverage with wind speed may be due to combined wind and wave state conditions encountered in the Gulf of Tehuantepec. The lower wind speeds generally occurred in more fully developed seas, as shown by the color in Fig. 8. Other field studies have shown that whitecap coverage decreases with sea state (Lafon et al. 2004, 2007; Sugihara et al. 2007). Furthermore, in the lower wind speed conditions, the wind has been decreasing with fetch. The wind history has been shown to affect the wave development and whitecap coverage (Hanson and Phillips 1999; Callaghan et al. 2008b).

The steep trend of the whitecap coverage with wind speed may be affected by image processing methodology as well. As mentioned, a relatively strict brightness threshold was needed to avoid false classification of foam patches. Waves breaking under light winds are generally smaller and dimmer and are more difficult to

detect with a single brightness threshold. While the small, dim breakers would go equally undetected in all conditions, they contribute a greater fraction to the whitecap coverage at low wind speeds. Furthermore, all of the studies in Fig. 8 except Bondur and Sharkov (1982) are from cameras mounted on a research vessel, platform, or tower, observing the ocean from oblique angles. Images captured at oblique angles incorporate serious distortions of the sea surface, which to our knowledge are not corrected in estimating whitecap coverage. Each image contains a wide range of resolution, as a function of distance to the camera, making determination of resolution issues difficult.

b. Comparison of observed $\Lambda(c)$ distributions to Phillips’s formulation

Figure 2g shows a comparison of the Phillips model for $\Lambda(c)$ [Eq. (6); dotted–dashed line] to the observed $\Lambda(c)$ distributions. A closer look at this comparison is presented in this section. We consider the values of the coefficient $(4\gamma\beta^3)I(3p)$ from the Phillips model in Eqs. (6) and (7). Toba’s (1973) parameter α can be related to the coefficients β and p by

$$\alpha = 4\beta I(p) \tag{32}$$

from the expression for the equilibrium wave frequency spectra derived in the Phillips theory.

From comparison of the spectral wind input function to the spectral wave action dissipation function, Phillips (1985) estimates that $\gamma\beta^2$ should be somewhat larger than the wind–wave coupling coefficient, $m \approx 0.04$. Simply taking $\gamma\beta^2 = 0.04$ along with (32), the coefficient $(4\gamma\beta^3)I(3p)$ can be expressed as $m\alpha I(3p)/I(p)$.

From previous field studies, Phillips (1985) estimated that $0.06 < \alpha < 0.11$, which is in good agreement with the wave observations from the GOTEX (Romero and Melville 2010a), where the relationship

$$\alpha = (0.016)(c_p/u_{*e})^{0.53 \pm 0.02}$$

was found. Phillips suggested that p is in the range of 0.5–2, most probably toward the smaller values. Our observations of $\hat{\Lambda}(\theta)$ also support a smaller value of p , such as 0.5 (Fig. 6). Regardless, $I(3p)/I(p)$ varies only from 0.73 to 0.62 as p increases from 0.5 to 2. Thus, the coefficient $(4\gamma\beta^3)I(3p) = m\alpha I(3p)/I(p)$ falls in the range of 0.0015–0.0032, with a central value of 0.0024.

In Fig. 2g, the lower black dotted–dashed line corresponds to $(4\gamma\beta^3)I(3p) = 0.0015$ and the lowest friction velocity u_{*e} obtained at the image sequences. The upper black dotted–dashed line corresponds to a coefficient of 0.0032 and the highest friction velocity. All of the models

use the value for the breaking parameter $b = 0.06$, as suggested by Phillips (1985), based on the quasi-steady breaking experiments by Duncan (1981). However, we know that the breaking strength parameter is at least dependent on a characteristic wave slope parameter (Melville 1994; Banner and Peirson 2007; Drazen et al. 2008).

For the faster speeds of breaking ($c > 5 \text{ m s}^{-1}$), the observed $\Lambda(c)$ distributions appear to follow a trend similar to c^{-6} , but are well above the Phillips model. The offset may be attributed to the breaking parameter b . A smaller value of b , such as $b = 10^{-2}$ to 10^{-3} brings the Phillips formulation into rough agreement with the observations. Here $\Lambda(c)$ shows the closest qualitative agreement to the Phillips formulation for speeds greater than 5 m s^{-1} . The majority of breaking occurs near the peak of $\Lambda(c)$.

The $\Lambda(c)$ distributions in Fig. 2g suggest a qualitatively favorable comparison of the observations to the Phillips formulation (6) for higher speeds ($c > 5 \text{ m s}^{-1}$), with potentially large errors due to lack of knowledge of various parameters. Are the $\Lambda(c)$ observations well described by a power law function? If so, what is the power law and what are reasonable coefficients? To answer this question, we use the expression (6) to nondimensionalize $\Lambda(c)$:

$$\Lambda(c)u_{*e}^3g^{-1}\left(\frac{c}{u_{*e}}\right)^6 = (4\gamma\beta^3b^{-1})I(3p). \tag{33}$$

The results are shown in Fig. 12a. The equilibrium range is taken as $c_T < c < 0.7c_p$, where c_T is the phase speed corresponding to the wavenumber k_T at which the wave spectrum transitions from a -2.5 to -3 power law dependence, as discussed in section 1. The equilibrium range is mapped to $0 < \hat{c} < 1$, where

$$\hat{c} = \frac{(c - c_T)}{(c_o - c_T)} \tag{34}$$

and

$$c_o = 0.7c_p, \tag{35}$$

marked by vertical black lines in Fig. 12a. The horizontal dashed–dotted lines represent the rhs of (33) using $b = 0.06$, $p = 0.5$, the wind–wave coupling coefficient $m = \gamma\beta^2 = 0.04$, and Toba parameter $\alpha = 4\beta I(p)$ in the range of 0.06–0.11.

If the Phillips formulation, Eq. (6), is a good model for our observations, we would expect to see the data collapse to a horizontal line in the dimensionless coordinates. Some of the observations appear roughly horizontal in Fig. 12a. However, this generally occurs at speeds larger than $c_o = 0.7c_p$, which corresponds to wavenumbers at and below the spectral peak region, where the equilibrium

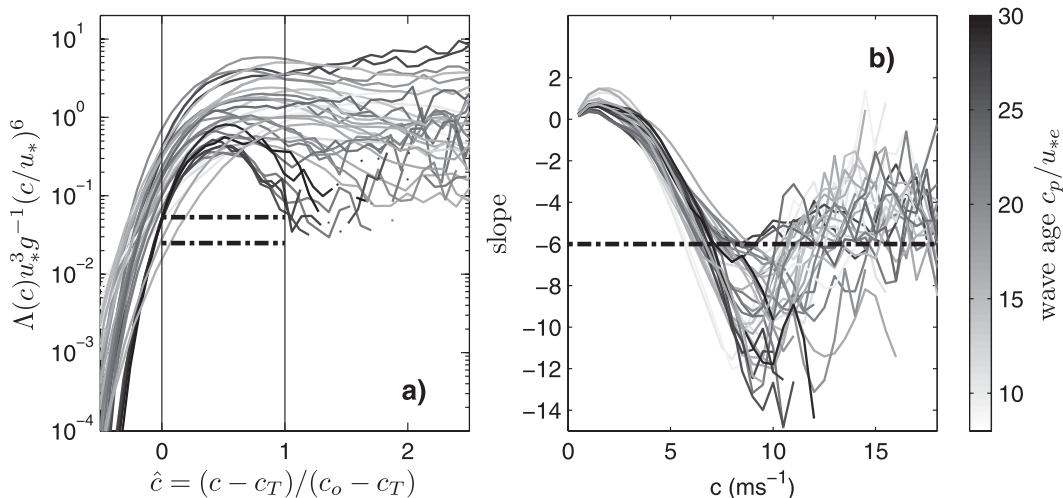


FIG. 12. (a) $\Lambda(c)$ nondimensionalized as in Eq. (33). The abscissa is scaled so that 0 corresponds to the phase speed at which the omnidirectional spectra transitions from a -2.5 to a -3 power law and 1 corresponds to $c_o = 0.7c_p$ at the location of each $\Lambda(c)$ observation. Horizontal dashed–dotted lines indicate the range of coefficients in the Phillips formulation [Eq. (6)]. (b) The local power law slope of the $\Lambda(c)$ distributions calculated by Eq. (37). The horizontal black dashed–dotted line indicates the theoretical slope of the Phillips (1985) equilibrium formulation for $\Lambda(c)$ [Eq. (6)].

assumption is not valid. Within the equilibrium range $0 < \hat{c} < 1$, there is little evidence for a c^{-6} dependence of the $\Lambda(c)$ curves.

Is there any power law description of the observed $\Lambda(c)$ distributions? If we wish to find a description,

$$\Lambda(c) = Ac^n, \tag{36}$$

then we can solve for $n(c)$,

$$n(c) = \frac{d\ln(\Lambda(c))}{d\ln(c)}. \tag{37}$$

The slopes of the curves in Fig. 2 are computed according to (37). To reduce the noise of the slope estimate, the $\Lambda(c)$ distributions are convolved with a five-point triangular window before the difference is taken. The slopes are truncated at the high-speed noise floor, which is identified by the speed at which the slope of $\Lambda(c)$ changes by more than four orders of magnitude for neighboring values of c , with $\Delta c = 0.5 \text{ m s}^{-1}$. In Fig. 12b we see that the maximum value of $\Lambda(c)$ occurs where the slope is zero, at $1 < c < 4 \text{ m s}^{-1}$. The slope of the $\Lambda(c)$ distribution becomes more negative as the breaking speed increases until it levels off around $c = 8 \text{ m s}^{-1}$. The Phillips formulation [Eq. (6)] would have a slope of -6 , which is shown with the black dashed–dotted line. Attempts to fit a power law form to the observed $\Lambda(c)$ distributions are dependent on the range of speeds considered since the slope of the distribution is gradually changing, as indicated in Fig. 12b. The two regimes of

the $\Lambda(c)$ distribution, as noted in Fig. 4, are also seen in Fig. 12.

c. Rayleigh distribution fit to $\Lambda(c)$

After extensive testing, a better functional description of the observed $\Lambda(c)$ distributions was obtained. A Rayleigh distribution provides a reasonably good fit to the $\Lambda(c)$ distributions. A Rayleigh distribution is described by

$$p(x) = \frac{x}{s^2} \exp\left(\frac{-x^2}{2s^2}\right) \tag{38}$$

and

$$P(x) = 1 - \exp\left(\frac{-x^2}{2s^2}\right), \quad x > 0, \tag{39}$$

where $p(x)$ is the probability density function (pdf) and $P(x)$ is the cumulative distribution function (CDF). We propose that, over a significant range of c , the observed $\Lambda(c)$ distributions can be described by a function of the form

$$\frac{\Lambda(c)}{A} = \frac{(c + x_o)}{s^2} \exp\left(\frac{-(c + x_o)^2}{2s^2}\right) \tag{40}$$

and

$$A = \int_0^\infty \Lambda(c') dc'; \tag{41}$$

TABLE 1. The environmental parameters for the Gulf of Tehuantepec Experiment. Fields are (left)–(right) RF: the research flight, Alt: aircraft altitude, A_{TOT} : the nonoverlapping areal coverage of images (km^2), X_e : effective fetch (km); U_{10} : the 10-m wind speed; u_{*e} : the effective wind friction velocity, k_p : spectral peak wavenumber, W_T : thresholded whitecap coverage fraction, W_A : the active whitecap coverage fraction, \mathcal{R} : breaking rate, L_{peak} : the maximum value of the $\Lambda(c)$ distribution, $\mathcal{A} = \int \Lambda(c) dc$: integral of the $\Lambda(c)$ distribution, s : the Rayleigh parameter fit, x_o : the speed offset to the Rayleigh parameter fit, and c_1 and c_2 : speeds at which $\Lambda(c)$ obtains half its peak value.

RF	Alt (m)	A_{TOT} (km^2)	X_e (km)	U_{10} (m s^{-1})	u_{*e} (m s^{-1})	k_p (m^{-1})	W_T (%)	W_A (%)	\mathcal{R} (10^{-3} s^{-1})	L_{peak} (10^{-4} $\text{m}^{-2} \text{s}$)	\mathcal{A} (10^{-4}m^{-1})	s (m s^{-1})	x_o (m s^{-1})	c_1 (m s^{-1})	c_2 (m s^{-1})
5	364	3.3	210	17.2	0.65	0.057	1.32	1.03	11.7	7.9	34.1	2.6	0.0	0.9	5.0
5	376	3.2	340	15.5	0.72	0.053	0.95	0.68	5.5	3.9	15.7	2.4	0.0	0.9	4.6
5	377	2.5	380	15.0	0.66	0.047	0.59	0.48	4.2	2.6	10.9	2.6	-0.1	1.0	5.1
5	378	4.8	396	14.8	0.63	0.051	0.69	0.49	4.6	2.9	12.2	2.5	-0.1	0.9	4.8
5	368	4.3	352	17.4	0.62	0.056	0.71	0.47	3.9	2.3	10.2	2.7	0.0	0.9	5.1
5	384	4.4	238	16.5	0.79	0.056	0.37	0.27	2.8	1.1	6.4	3.3	0.0	1.0	6.4
5	373	3.6	63	19.8	0.62	0.098	0.46	0.32	3.1	2.5	8.9	2.2	-0.4	1.2	4.5
5	375	3.6	44	20.2	0.72	0.136	0.82	0.51	4.5	3.5	12.9	2.2	-0.3	1.0	4.5
5	399	3.3	7	17.3	0.73	0.215	1.47	1.08	11.0	6.7	29.0	2.7	-0.1	1.0	5.1
7	380	2.5	6	16.0	0.57	0.287	1.13	0.68	8.4	7.0	25.9	2.3	0.0	0.9	4.4
7	374	4.2	20	15.7	0.56	0.165	1.21	0.81	8.3	6.0	23.8	2.4	-0.1	0.9	4.7
7	375	3.2	41	15.2	0.55	0.115	0.89	0.65	7.2	4.2	17.5	2.6	-0.4	1.3	5.4
7	369	3.7	57	14.9	0.54	0.094	1.45	1.12	13.1	8.7	37.2	2.6	-0.1	0.9	5.1
7	371	3.7	196	13.3	0.46	0.063	0.45	0.29	4.1	3.8	14.8	2.4	0.3	0.6	4.3
7	376	3.7	214	13.0	0.47	0.062	0.55	0.38	5.2	4.5	18.1	2.4	0.3	0.5	4.4
10	357	3.1	37	17.2	0.57	0.114	1.03	0.77	10.5	7.1	31.4	2.7	0.1	0.7	5.1
10	368	4.2	53	17.4	0.66	0.098	1.62	1.33	16.1	9.7	44.1	2.7	0.1	0.7	5.1
10	369	3.2	92	18.1	0.76	0.071	1.04	0.85	8.3	4.5	22.2	2.8	0.1	0.7	5.4
10	371	4.2	108	17.9	0.74	0.064	1.08	0.83	7.0	4.1	18.7	2.7	0.1	0.7	5.2
10	360	1.8	155	16.8	0.70	0.053	0.21	0.18	1.9	0.8	4.1	2.9	0.0	0.9	5.6
10	358	4.8	179	16.2	0.67	0.050	0.33	0.24	2.5	1.7	7.8	2.8	0.5	0.5	4.9
10	356	3.2	214	15.2	0.63	0.051	0.17	0.12	1.1	0.6	2.6	2.6	-0.1	0.9	5.1
10	355	2.9	216	15.1	0.63	0.051	0.13	0.11	1.3	0.8	3.5	2.6	0.0	0.8	5.1
10	392	3.6	261	14.2	0.60	0.054	0.33	0.22	2.3	2.0	8.0	2.4	0.3	0.5	4.4
10	392	3.1	275	13.9	0.58	0.052	0.45	0.32	2.6	1.8	8.2	2.8	0.6	0.4	4.8
10	382	2.5	302	13.5	0.54	0.048	0.06	0.04	0.9	0.3	1.5	2.9	0.0	0.8	5.6
10	389	2.5	313	13.4	0.53	0.049	0.06	0.03	0.9	0.3	1.6	2.9	-0.2	1.0	5.8
10	387	2.5	325	13.3	0.51	0.049	0.09	0.06	0.8	0.4	1.6	2.8	0.1	0.7	5.4
10	369	3.5	365	13.4	0.48	0.050	0.11	0.07	1.3	0.4	1.7	3.0	0.0	0.9	5.8
10	368	3.4	381	13.1	0.46	0.048	0.08	0.04	0.9	0.3	1.3	2.7	-0.3	1.1	5.3
10	323	3.1	35	14.3	0.46	0.182	0.17	0.12	2.0	1.1	4.6	2.5	-0.1	0.9	5.0
10	373	3.6	47	14.5	0.52	0.128	0.24	0.14	2.3	1.1	4.9	2.7	-0.3	1.2	5.4

A scales $\Lambda(c)$ appropriately since the integral under a pdf is one and x_o is an offset to the breaking speed. Kleiss and Melville (2010) found that adjusting the observed breaking speed for underlying long wave orbital velocity and the presence of surface currents resulted in a net shift of the $\Lambda(c)$ distributions with respect to speed, which motivated consideration of the speed offset x_o . Although a Rayleigh distribution fits the data fairly well without the x_o parameter, the fits are improved with the offset included.

The integral A is calculated directly from the $\Lambda(c)$ observations. The parameters s and x_o are systematically varied from $1 < s < 4 \text{ m s}^{-1}$ and $-3 < x_o < 3 \text{ m s}^{-1}$, and the pair (s, x_o) is selected to minimize the mean square error between the empirical distribution and the Rayleigh distribution over the range $0 < c < 12 \text{ m s}^{-1}$.

The final values of s fall in the range $[2.1, 3.2] \text{ m s}^{-1}$, the speed offset x_o falls in the range $[-0.4, 0.6] \text{ m s}^{-1}$, and are given in Table 1.

Comparisons of the Rayleigh distribution fit to three sample $\Lambda(c)$ distributions are shown in the top row of Fig. 13, with the empirical $\Lambda(c)$ distributions shown in color and the minimum-error Rayleigh fit shown with circles. The distribution generally fits the data surprisingly well.

To visualize how well the $\Lambda(c)$ distributions agree with the Rayleigh distribution, we consider the normalized cumulative distribution [Eq. (39)]

$$\text{CDF} = \frac{\int_0^c \Lambda(c') dc'}{\int_0^\infty \Lambda(c') dc'} \quad (42)$$

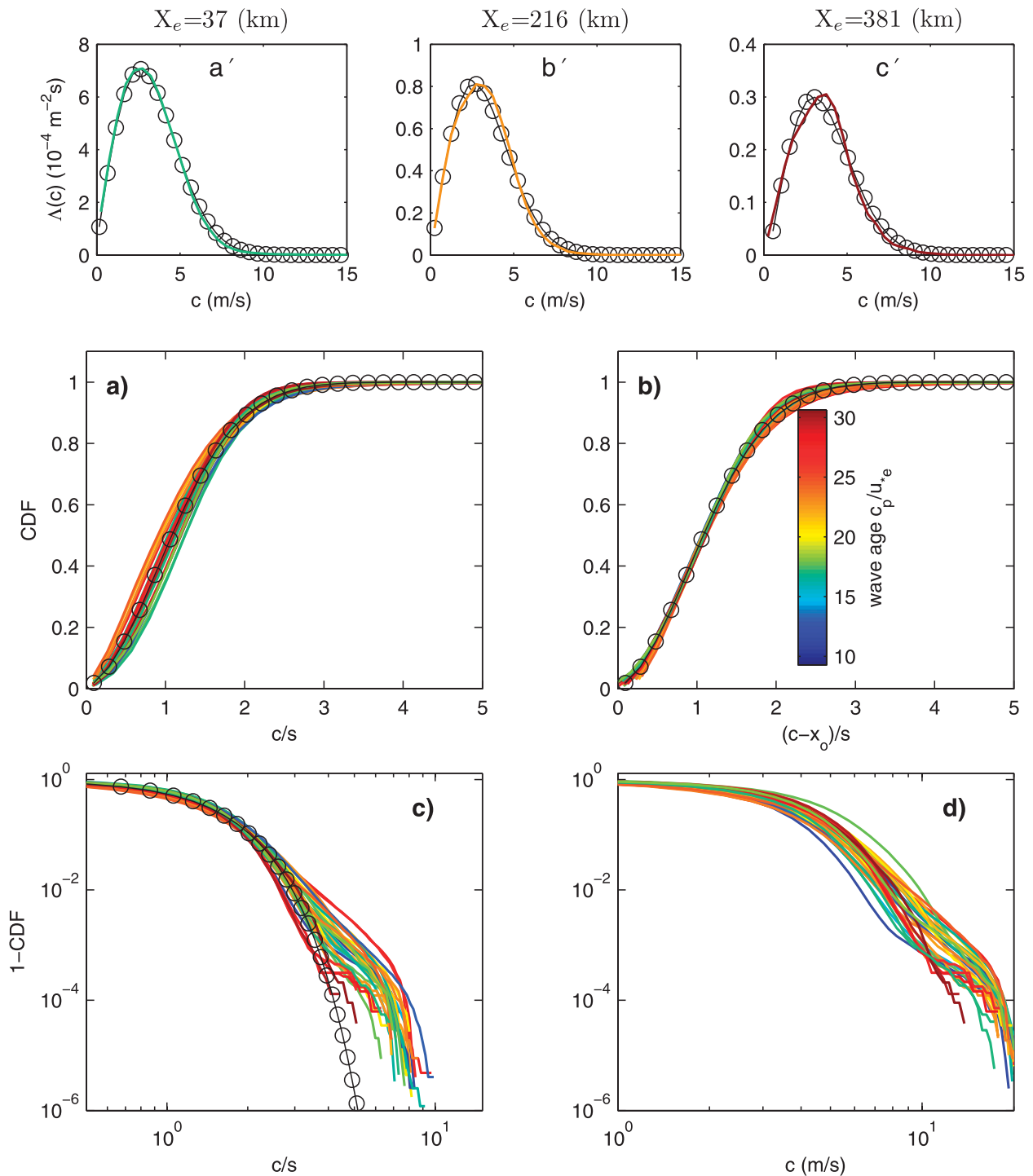


FIG. 13. (a')–(c') Examples of Rayleigh distribution fits to the $\Lambda(c)$ distributions [Eq. (40)]. Observed $\Lambda(c)$ distributions are shown with color corresponding to wave age, and lines with circles are the Rayleigh distributions, with amplitudes set by A [Eq. (41)], and the best fits of s and x_o over the range $0 < c < 12 \text{ m s}^{-1}$. The y axis has units of $10^{-4} \text{ m}^{-2} \text{ s}$. For the three examples the total length of breaking $A \times 10^4$ is 31.4, 8.0, and 1.3 m^{-1} . The s parameter is 2.7, 2.4, and 2.7 m s^{-1} . The x_o offset is 0.1, 0.3, and -0.3 m s^{-1} . (a)–(d) The normalized cumulative $\Lambda(c)$ distributions for (a) the breaking speed normalized by the Rayleigh parameter s , (b) breaking speed normalized by both s and the horizontal offset x_o , (c) one minus the normalized cumulative distribution vs normalized speed in logarithmic coordinates, and (d) one minus the normalized cumulative distribution vs dimensional speed. Line color indicates effective wave age, and the black line with circles shows the reference Rayleigh distribution.

The observed $\Lambda(c)$ normalized cumulative distributions are shown in color in Fig. 13. The speed of breaking is normalized by s in Figs. 13a,c and $(c - x_o)/s$ in Fig. 13b. A true normalized Rayleigh cumulative distribution, $1 - \exp(-c^2/2s^2)$, is shown by the black line with circles. The observations show good agreement with the Rayleigh distributions in Figs. 13a,b. To examine the high-speed range more closely, one minus the cumulative distribution function is presented in Figs. 13c,d in logarithmic coordinates. For normalized speeds above 3, corresponding to breaking speeds of 7–10 m s⁻¹, the distributions begin to deviate from the Rayleigh function. One minus the cumulative distribution is shown versus dimensional speed in Fig. 13d for reference. The enhanced levels of $\Lambda(c)$ at high speeds are also evident in the raw distributions (Fig. 2), the higher moments of $\Lambda(c)$ (Fig. 4), and the power law slope of the $\Lambda(c)$ distributions (Fig. 12b).

The description of $\Lambda(c)$ as a Rayleigh distribution is found empirically. A Rayleigh distribution may be derived for the modulus of a two-dimensional vector field with components that are normally distributed, are uncorrelated, and have equal variance. The directional $\Lambda(c)$ distributions in Fig. 5 did not indicate that the velocity components were normally distributed. However, at the smaller values of c the $\Lambda(c, \theta)$ distributions broaden and sometimes exhibit a bimodality, both of which could be indicative of independent and orthogonal velocity components. Wave elevation directional spectra also show that the spectra broadens for larger wavenumber (smaller speeds), exhibiting almost orthogonal bimodality.

From the sensitivity studies presented in Kleiss and Melville (2010), we recognize that the $\Lambda(c)$ distributions at low speeds are more sensitive to the observational resolution and to the processing thresholds. This is related to the fact that smaller, slower breaking waves do not entrain as many bubbles, so they have less contrast in visible images. Owing to the lack of bright foam, our processing may miss the smaller breaking waves, which presumably are breaking with the slower speeds. The ability to resolve small breaking waves with minimal or no bubble entrainment may dramatically affect the $\Lambda(c)$ distributions for smaller speeds, affecting the appropriateness of the Rayleigh distribution as a description of $\Lambda(c)$.

The parameters describing the Rayleigh fit to the data [Eq. (40)] basically describe the amplitude of the $\Lambda(c)$ distribution A , the width s , and the offset in speed x_o . The width of $\Lambda(c)$ can also be estimated directly from the $\Lambda(c)$ distributions, without assuming the $\Lambda(c)$ distributions follow a Rayleigh distribution. Figure 14a shows one $\Lambda(c)$ distribution. The width is determined by the values of $\Lambda(c)$ at one-half its maximum.

The amplitude and width descriptors of $\Lambda(c)$ are considered in the context of the fetch-limited conditions observed in the Gulf of Tehuantepec. Although both wind speed and direction changed gradually with fetch, the wave energy and spectral peak frequency agree with the classical fetch relations as given by Kahma and Calkoen (1992) after nondimensionalization by the effective friction velocity u_{*e} and gravity g (Romero and Melville 2010a, Fig. 7). The decaying wind speed with fetch does not affect the fetch-limited wave conditions encountered in the Gulf of Tehuantepec. The dimensional analysis in section 4b indicated that the $\Lambda(c)$ distribution is expected to be a function of the dimensionless breaking speed and the nondimensional fetch. Using the peak wave parameters to nondimensionalize $\Lambda(c)$ did not collapse the data, but introduced more of a trend (Fig. 3). Therefore, we nondimensionalize the $\Lambda(c)$ scaling parameters using the friction velocity u_{*e} and gravity g and compare to the nondimensional fetch χ . The units of A are L⁻¹, and s and x_o have units of LT⁻¹. It follows that the dimensionless forms are $Au_{*e}^2g^{-1}$, su_{*e}^{-1} , and $x_o u_{*e}^{-1}$. These nondimensional variables are compared to the nondimensional fetch in Fig. 14.

Figure 14d shows that the total length of breaking per unit sea surface area, nondimensionalized with friction velocity and gravity, decreases with nondimensional fetch. The solid line shows a least squares fit in logarithmic coordinates, $Au_{*e}^2g^{-1} = 0.25\chi^{-0.56}$. Meanwhile, the nondimensional width of the $\Lambda(c)$ distribution increases very weakly, like $s/u_{*e} = 1.69\chi^{0.06}$. The speed offset x_o is also shown in dimensionless coordinates for completeness. Generally x_o is less than the local friction velocity, which is 0.46–0.79 m s⁻¹. This is consistent with the idea that the speed may be affected by surface drift currents, resulting in a shift of the $\Lambda(c)$ distributions, as seen in Kleiss and Melville (2010).

The actual width of the $\Lambda(c)$ distributions, $(c_2 - c_1)$, depends on an arbitrarily chosen level, at 50% of the maximum value of $\Lambda(c)$, but its meaning is straightforward to interpret. The Rayleigh width s results from the shape of the entire $\Lambda(c)$ distribution, but it depends on the empirical description of $\Lambda(c)$ as a Rayleigh distribution. It lends confidence to both measures that the trend of the actual width in Fig. 14b appears very similar to the Rayleigh parameter s and increases weakly with dimensionless fetch, $(c_2 - c_1)/u_{*e} = 2.48\chi^{0.07}$. Figure 14c shows that most (85%) of the increase in the width is due to changes in the upper speed c_2 , which increases with fetch like $(c_2/u_{*e} = 3.64\chi^{0.06})$. The lower speed does not show a trend with dimensionless fetch ($c_1/u_{*e} = 1.58\chi^{-0.01}$). This is akin to the fetch-limited evolution of the wave elevation spectra. The spectra at high wavenumbers (slow phase speed) do not evolve with fetch once the saturation range

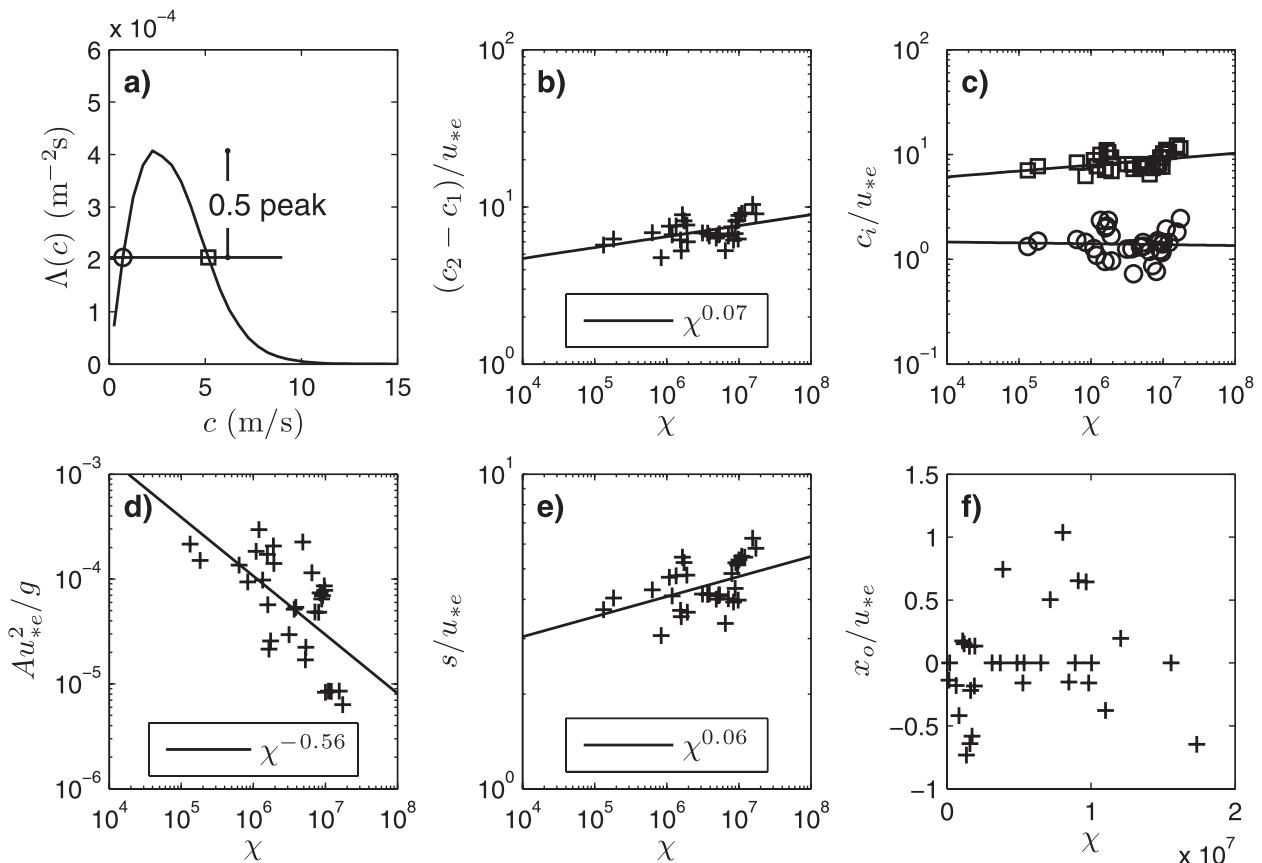


FIG. 14. (a)–(c) Geometrical parameters and (d)–(f) nondimensionalized Rayleigh parameters describing the $\Lambda(c)$ distributions plotted against dimensionless fetch: c_1 and c_2 are the low- and high-speed endpoints of the width of the $\Lambda(c)$ distributions and are shown in (c) with circles and squares, respectively. A is the total length of breaking per unit sea surface area, s is the Rayleigh parameter, and x_o is a speed offset.

is reached, while the active spectral evolution occurs at low wavenumbers (fast phase speed).

From analysis of the wave elevation spectra (Romero and Melville 2010a), the best fit to the observed fetch relation for peak frequency is

$$\hat{f}_p = 0.28\chi^{-0.25}, \quad (43)$$

where $\hat{f}_p = f_p u_{*e}/g$ is the nondimensional peak frequency with f_p in cycles per unit time. Transforming (43) from f_p to c_p using the deep water dispersion relation,

$$\frac{c_p}{u_{*e}} = 0.57(\chi)^{0.25}, \quad (44)$$

describes the evolution of the spectral peak phase speed with fetch. The evolution of the upper speed c_2 in Fig. 14c is

$$\frac{c_2}{u_{*e}} = 3.64(\chi)^{0.06}. \quad (45)$$

Combining Eqs. (44) and (45), we expect the ratio of the faster speeds of breaking to the spectral peak phase speed to decrease with dimensionless fetch as

$$\frac{c_2}{c_p} = 7.2(\chi)^{-0.19}. \quad (46)$$

Likewise, the evolution of the Rayleigh parameter s with dimensionless fetch χ results in

$$\frac{s}{c_p} = 3.4(\chi)^{-0.19}. \quad (47)$$

The observed values of c_2/c_p , as well as the expression (46), are presented in Fig. 15 in linear (Figs. 15a,c) and logarithmic (Figs. 15b,d) coordinates. Many previous field studies have observed that wave breaking occurs near the peak phase speed for young seas and decreases with wave age (Ding and Farmer 1994; Melville 1994; Felizardo and Melville 1995; Banner et al. 2002; Gemmrich et al. 2008). Equation (46) provides a more quantitative description

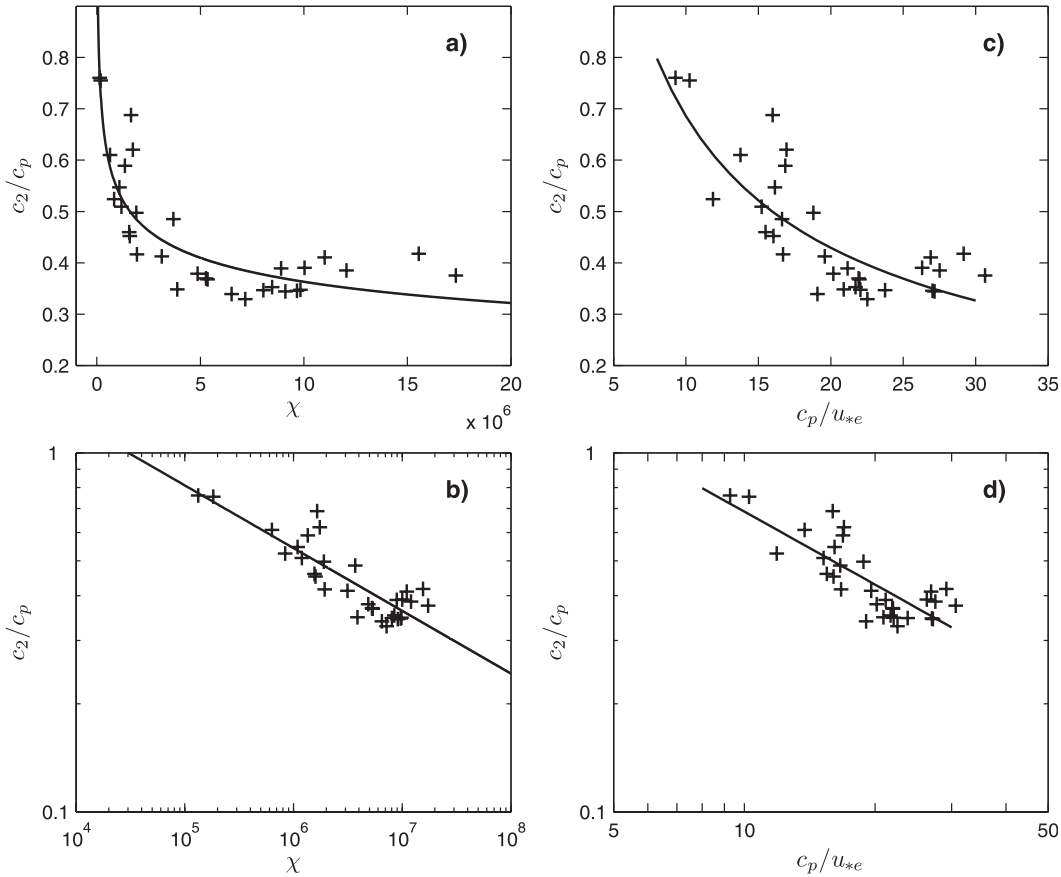


FIG. 15. The ratio of the upper speed c_2 , at which $\Lambda(c)$ falls to half its maximum value, to the spectral peak phase speed c_p as a function of (a),(b) dimensionless fetch χ and (c),(d) effective wave age. The black line in (a),(b) shows Eq. (46). In (c),(d), the black line is a fit to the data, $c_2/c_p = 3.26(c_p/u_{*e})^{-0.68}$. Note logarithmic ordinate for (c) and (d).

of the ratio of the observed speeds of breaking to the dominant phase speed as a function of dimensionless fetch.

6. Summary

Video observations of ocean surface wave breaking were obtained from fetch-limited conditions under strong (10–25 m s⁻¹) winds. The distribution of the length of breaking crests per unit sea surface area, according to their breaking speed $\Lambda(c)$, is calculated from the image sequences and reported for the range of environmental conditions encountered. The nondimensionalized $\Lambda(c)$ distributions showed a consistent functional form that initially appears similar to a c^{-6} function for larger values of c , as suggested by Phillips’s (1985) model; however, on closer inspection the agreement with the Phillips model is tenuous because the range of c in which $\Lambda \propto c^{-6}$ is limited and not generally within the equilibrium range defined by Phillips. Various combinations of field parameters are

explored to describe the observed $\Lambda(c)$ distributions. The high-speed ($c > 10u_{*e}$) region appears to collapse with combinations of wind and wave variables, but the peak regions of the $\Lambda(c)$ distributions did not. This variability may be due to effects other than wind and wave states such as surface currents, surface current divergence, surface stability, and turning winds.

When scaled with the dominant spectral wave quantities, the $\Lambda(c)$ distributions show that some breaking is observed near the spectral peak for young (strongly forced) seas, whereas almost no breaking occurs at speeds above 75% of the dominant phase speed for well-developed seas. This is also apparent in the directional $\Lambda(c)$ distributions, which also show that wave breaking is more closely aligned with the wind direction than the dominant wave direction. From our analysis, the widest angular distribution of breaking occurs at the slower speeds, and the angular distribution becomes more narrow as breaking speed increases, generally consistent with the wavenumber dependence of the directional wave spectrum

(Romero and Melville 2010a). Both the magnitude of the $\Lambda(c)$ distributions and the width of the directional distribution collapse better with the wind magnitude and direction than with wave properties.

The whitecap coverage is computed and compared to the 10-m wind speed, friction velocity, wave age, and slope. The rate of breaking versus spectral peak steepness compares well with previous studies.

Close inspection of the observed $\Lambda(c)$ distributions indicates that the continuously changing slope of the $\Lambda(c)$ distribution is not easily described as a power law function of constant exponent. The $\Lambda(c)$ distributions do closely approximate a Rayleigh distribution when normalized by the integral of $\Lambda(c)$. The collapsing parameters, namely the width of the $\Lambda(c)$ distribution and the total length of breaking per sea surface area, show a weak dependence on nondimensional fetch. The increase in dimensionless width of $\Lambda(c)$ with dimensionless fetch compares well with the observed fetch relations and observations of wave breaking near the spectral peak.

The omnidirectional $\Lambda(c)$ is an azimuthal average of the full $\Lambda(\mathbf{c})$ distribution. A Rayleigh distribution could result from a two-dimensional Gaussian distribution of $\Lambda(\mathbf{c})$. Although the two-dimensional distributions are not easily described by Gaussian distributions (Fig. 5), Gaussian noise in the slower speeds may contribute to the observed Rayleigh distribution. Speeds less than 2 m s^{-1} are dependent on subpixel accuracy of the crest location and speed calculations. It should also be emphasized that the Rayleigh distribution results only for a specific processing method for $\Lambda(c)$: using the elemental speeds that are a function of both space and time and, in particular, taking the component of speed that is normal to the breaking crest (or equivalently along the brightness gradient). Calculations of $\Lambda(c)$ that use translational rather than normal speeds or that use temporal or event definitions of length and speed of breaking can only be described by the Rayleigh distribution with an offset in the speeds, x_o .

The biggest quantitative and qualitative differences between the Phillips (1985) model for $\Lambda(c)$ and our observations occur at speeds below the peak of the $\Lambda(c)$ distribution. Careful analysis of the effect of image resolution on the $\Lambda(c)$ distribution showed that higher image resolution shifted the peak to lower speeds but not at a rate that would converge to a speed of zero at infinite resolution. The GOTEX observed wave breaking that generated a patch of bubbles, with breaking duration longer than $2/3 \text{ s}$ and bubble patch size larger than 0.5 m^2 . Small-scale breaking on the ocean surface may not entrain air bubbles. Accurate estimation of the $\Lambda(c)$ distributions at low speeds needs to be addressed with high-resolution observations as well as the ability to observe wave breaking at microscales.

Acknowledgments. We acknowledge the collaboration of Carl A. Friehe (co-chief scientist of the GOTEX project) and Djamel Khelif at the University of California, Irvine. We are grateful to Allen Schanot, Henry Boynton, Lowell Genzlinger, Ed Ringleman, and support staff at NCAR Research Aviation Facility. We thank Bill Krabill, Bob Swift, Jim Yungel, John Sonntag, and Robbie Russell at NASA EG&G for the deployment and data postprocessing of the ATM. We are grateful to Leonel Romero for providing the processed wind and wave data. We thank Peter Matusov for helpful comments and discussions in the initial stages of this work. We thank two anonymous reviewers for comments that improved the quality of this manuscript. We acknowledge the assistance of Jim Lasswell and Axel Pierson at Scripps Institution of Oceanography. This research was supported by grants to WKM from the National Science Foundation (Ocean Sciences) and ONR (Physical Oceanography). JMK was also supported through the NSF Graduate Student Fellowship and National Defense Science and Engineering Graduate Student Fellowship.

REFERENCES

- Angelova, M. D., and F. Webster, 2006: Whitecap coverage from satellite measurements: A first step toward modeling the variability of oceanic whitecaps. *J. Geophys. Res.*, **111**, C03017, doi:10.1029/2005JC003158.
- Asher, W. E., and R. Wanninkhof, 1998: The effect of bubble-mediated gas transfer on purposeful dual-gaseous tracer experiments. *J. Geophys. Res.*, **103** (C5), 10 555–10 560.
- , J. Edson, W. McGillis, R. Wanninkhof, D. T. Ho, and T. Litchendorf, 2002: Fractional area whitecap coverage and air-sea gas transfer velocities measured during GasEx-98. *Gas Transfer at Water Surfaces*, *Geophys. Monogr.*, Vol. 127, Amer. Geophys. Union, 199–203.
- Babanin, A. V., I. R. Young, and M. L. Banner, 2001: Breaking probabilities for dominant surface waves on water of finite constant depth. *J. Geophys. Res.*, **106** (C6), 11 659–11 676.
- Banner, M. L., 1990: Equilibrium spectra of wind waves. *J. Phys. Oceanogr.*, **20**, 966–984.
- , and O. M. Phillips, 1974: On the incipient breaking of small scale waves. *J. Fluid Mech.*, **65**, 647–656.
- , and D. H. Peregrine, 1993: Wave breaking in deep water. *Annu. Rev. Fluid Mech.*, **25**, 373–397.
- , and W. L. Peirson, 2007: Wave breaking onset and strength for two-dimensional deep-water wave groups. *J. Fluid Mech.*, **585**, 93–115, doi:10.1017/S0022112007006568.
- , A. V. Babanin, and I. R. Young, 2000: Breaking probability for dominant waves on the sea surface. *J. Phys. Oceanogr.*, **30**, 3145–3160.
- , J. R. Gemmrich, and D. M. Farmer, 2002: Multiscale measurements of ocean wave breaking probability. *J. Phys. Oceanogr.*, **32**, 3364–3375.
- Bondur, V. G., and E. A. Sharkov, 1982: Statistical properties of whitecaps on a rough sea. *Oceanology*, **22**, 274–279.
- Brown, E. N., C. A. Friehe, and D. H. Lenschow, 1983: The use of pressure fluctuations on the nose of an aircraft for measuring air motion. *J. Climate Appl. Meteor.*, **22**, 171–180.

- Callaghan, A. H., G. B. Deane, and M. D. Stokes, 2008a: Observed physical and environmental causes of scatter in whitecap coverage values in a fetch-limited coastal zone. *J. Geophys. Res.*, **113**, C05022, doi:10.1029/2007JC004453.
- , G. de Leeuw, L. Cohen, and C. D. O'Dowd, 2008b: Relationship of oceanic whitecap coverage to wind speed and wind history. *Geophys. Res. Lett.*, **35**, L23609, doi:10.1029/2008GL036165.
- Caulliez, G., V. Makin, and V. Kudryavtsev, 2008: Drag of the water surface at very short fetches: Observations and modeling. *J. Phys. Oceanogr.*, **38**, 2038–2055.
- Chelton, D. B., M. H. Freilich, and S. K. Esbensen, 2000: Satellite observations of the wind jets off the Pacific coast of Central America. *Mon. Wea. Rev.*, **128**, 1993–2043.
- Ding, L., and D. M. Farmer, 1994: Observations of breaking surface wave statistics. *J. Phys. Oceanogr.*, **24**, 1368–1387.
- Donelan, M. A., F. W. Dobson, S. D. Smith, and R. J. Anderson, 1993: On the dependence of sea surface roughness on wave development. *J. Phys. Oceanogr.*, **23**, 2143–2149.
- Drazen, D. A., W. K. Melville, and L. Lenain, 2008: Inertial scaling of dissipation in unsteady breaking waves. *J. Fluid Mech.*, **611**, 307–332.
- Duncan, J. H., 1981: An experimental investigation of breaking waves produced by a towed hydrofoil. *Proc. Roy. Soc. London*, **377A**, 331–348.
- Eifler, W., 2005: The near-surface boundary layer. *Marine Turbulence*, H. Z. Baumert, J. H. Simpson, and J. Sündermann, Eds., Cambridge University Press, 250–272.
- Felizardo, F. C., and W. K. Melville, 1995: Correlations between ambient noise and the ocean surface wave field. *J. Phys. Oceanogr.*, **25**, 513–532.
- Gemmrich, J. R., and D. M. Farmer, 1999: Observations of the scale and occurrence of breaking surface waves. *J. Phys. Oceanogr.*, **29**, 2595–2606.
- , M. L. Banner, and C. Garrett, 2008: Spectrally resolved energy dissipation rate and momentum flux of breaking waves. *J. Phys. Oceanogr.*, **38**, 1296–1312.
- Gonzalez-Silvera, A., E. Santamaria-del-Angel, R. Millán-Nuñez, and H. Manzo-Monroy, 2004: Satellite observations of meso-scale eddies in the Gulfs of Tehuantepec and Papagayo (eastern tropical Pacific). *Deep-Sea Res. II*, **51**, 587–600.
- Hanson, J. L., and O. M. Phillips, 1999: Wind sea growth and dissipation in the open ocean. *J. Phys. Oceanogr.*, **29**, 1633–1648.
- Hasselmann, K., and Coauthors, 1973: Measurements of wind-wave growth and swell decay during the Joint North Sea Wave Project (JONSWAP). *Dtsch. Hydrogr. Z.*, **8**, 1–95.
- Holthuijsen, L. H., and T. H. C. Herbers, 1986: Statistics of breaking waves observed as whitecaps in the open sea. *J. Phys. Oceanogr.*, **16**, 290–297.
- Hwang, P. A., and D. W. Wang, 2001: Directional distributions and mean square slopes in the equilibrium and saturation ranges of the wave spectrum. *J. Phys. Oceanogr.*, **31**, 1346–1360.
- Jessup, A. T., and K. R. Phadnis, 2005: Measurement of the geometric and kinematic properties of microscale breaking waves from infrared imagery using a PIV algorithm. *Meas. Sci. Technol.*, **16**, 1961–1969.
- Jones, I. S. F., and Y. Toba, 2001: *Wind Stress over the Ocean*. Cambridge University Press, 326 pp.
- Kahma, K. K., and C. J. Calkoen, 1992: Reconciling discrepancies in the observed growth of wind-generated waves. *J. Phys. Oceanogr.*, **22**, 1389–1405.
- Katsaros, K. B., and S. S. Ataktürk, 1992: Dependence of wave-breaking statistics on wind stress and wave development. *Breaking Waves*, M. L. Banner and R. H. J. Grimshaw, Eds., Springer, 119–132.
- Kennedy, R. M., and R. L. Snyder, 1983: On the formation of whitecaps by a threshold mechanism. Part II: Monte Carlo experiments. *J. Phys. Oceanogr.*, **13**, 1493–1504.
- Kitaigorodskii, S. A., 1962: Applications of the theory of similarity to the analysis of wind-generated wave motion as a stochastic process. *Izv. Akad. Nauk SSSR, Ser. Geofiz.*, **1**, 105–117.
- Kleiss, J. M., 2009: Airborne observations of the kinematics and statistics of breaking waves. Ph.D. dissertation, University of California, San Diego, 219 pp.
- , and W. K. Melville, 2011: The analysis of sea surface imagery for white cap kinematics. *J. Atmos. Oceanic Technol.*, in press.
- Kraan, C., W. A. Oost, and P. A. E. M. Janssen, 1996: Wave energy dissipation by whitecaps. *J. Atmos. Oceanic Technol.*, **13**, 262–267.
- Krabill, W. B., and C. F. Martin, 1987: Aircraft positioning using global positioning system carrier phase data. *Navigation*, **34**, 1–21.
- Lafon, C., J. Piazzola, P. Forget, O. Le Calve, and S. Despiau, 2004: Analysis of the variations of the whitecap fraction as measured in a coastal zone. *Bound.-Layer Meteor.*, **111**, 339–360.
- , —, —, and S. Despiau, 2007: Whitecap coverage in coastal environment for steady and unsteady wave field conditions. *J. Mar. Syst.*, **66**, 38–46.
- Lamarre, E., and W. K. Melville, 1992: Instrumentation for the measurement of void-fraction in breaking waves: Laboratory and field results. *IEEE J. Oceanic Eng.*, **17**, 204–215.
- Longuet-Higgins, M. S., 1978: The instabilities of gravity waves of finite amplitude in deep water. I. Superharmonics. *Proc. Roy. Soc. London*, **360A** (1703), 471–488.
- , and N. D. Smith, 1983: Measurement of breaking waves by a surface jump meter. *J. Geophys. Res.*, **88** (C14), 9823–9831.
- Makin, V. K., and V. N. Kudryavtsev, 2002: Impact of dominant waves on sea drag. *Bound.-Layer Meteor.*, **103**, 83–99.
- Manasseh, R., A. V. Babanin, C. Forbes, K. Rickards, I. Bobevski, and A. Ooi, 2006: Passive acoustic determination of wave-breaking events and their severity across the spectrum. *J. Atmos. Oceanic Technol.*, **23**, 599–618.
- Melville, W. K., 1994: Energy dissipation by breaking waves. *J. Phys. Oceanogr.*, **24**, 2041–2049.
- , 1996: The role of surface-wave breaking in air-sea interaction. *Annu. Rev. Fluid Mech.*, **28**, 279–321.
- , and R. Rapp, 1985: Momentum flux in breaking waves. *Nature*, **317**, 514–516.
- , and P. Matusov, 2002: Distribution of breaking waves at the ocean surface. *Nature*, **417**, 58–63.
- Mironov, A. S., and V. A. Dulov, 2008: Detection of wave breaking using sea surface video records. *Meas. Sci. Technol.*, **19**, 015405, doi:10.1088/0957-0233/19/1/015405.
- Monahan, E. C., 1971: Oceanic whitecaps. *J. Phys. Oceanogr.*, **1**, 139–144.
- , 1993: Occurrence and evolution of acoustically relevant subsurface bubble plumes and their associated, remotely monitorable, surface whitecaps. *Natural Physical Sources of Underwater Sound*, Kerman, B. R., Ed., Springer, 503–517.
- , and C. R. Zietlow, 1969: Laboratory comparisons of freshwater and saltwater whitecaps. *J. Geophys. Res.*, **74**, 6961–6966.
- , and I. G. O'Muircheartaigh, 1986: Whitecaps and the passive remote sensing of the ocean surface. *Int. J. Remote Sens.*, **7**, 627–642.
- , and D. K. Woolf, 1989: Comments on "Variations of whitecap coverage with wind stress and water temperature." *J. Phys. Oceanogr.*, **19**, 706–709.

- , P. A. Bowyer, D. M. Doyle, M. R. Higgins, and D. K. Woolf, 1985: White-caps and the marine atmosphere. University College, Galway, Ireland, Rep. 5, 124 pp.
- Myrhaug, D., and L. E. Holmedal, 2008: Effects of wave age and air stability on whitecap coverage. *Coastal Eng.*, **55**, 959–966.
- Nordeng, T. E., 1991: On the wave age dependent drag coefficient and roughness length at sea. *J. Geophys. Res.*, **96** (C4), 7167–7174.
- Palacios, D. M., and S. J. Bograd, 2005: A census of Tehuantepec and Papagayo eddies in the northeastern tropical Pacific. *Geophys. Res. Lett.*, **32**, L23606, doi:10.1029/2005GL024324.
- Phillips, O. M., 1977: *The Dynamics of the Upper Ocean*. 2nd ed. Cambridge University Press, 336 pp.
- , 1985: Spectral and statistical properties of the equilibrium range in wind-generated gravity waves. *J. Fluid Mech.*, **156**, 505–531.
- , and M. L. Banner, 1974: Wave breaking in the presence of wind drift and swell. *J. Fluid Mech.*, **66**, 625–640.
- , F. L. Posner, and J. P. Hansen, 2001: High range resolution radar measurements of the speed distribution of breaking events in wind-generated ocean waves: Surface impulse and wave energy dissipation rates. *J. Phys. Oceanogr.*, **31**, 450–460.
- Rapp, R. J., and W. K. Melville, 1990: Laboratory measurements of deep-water breaking waves. *Philos. Trans. Roy. Soc. London*, **331A**, 735–780.
- Reising, S. C., W. E. Asher, L. A. Rose, and M. A. Aziz, 2002: Passive polarimetric remote sensing of the ocean surface: The effects of surface roughness and whitecaps. *Proc. Int. Union of Radio Science*, Maastricht, Netherlands, URSI General Assembly.
- Reul, N., and B. Chapron, 2003: A model of sea-foam thickness distribution for passive microwave remote sensing applications. *J. Geophys. Res.*, **108**, 3321, doi:10.1029/2003JC001887.
- Robles-Jarer, E. G., and J. R. Lara-Lara, 1993: Phytoplankton biomass and primary productivity by size classes in the Gulf of Tehuantepec, Mexico. *J. Plankton Res.*, **15**, 1341–1358.
- Romero, L., and W. K. Melville, 2010a: Airborne observations of fetch-limited waves in the Gulf of Tehuantepec. *J. Phys. Oceanogr.*, **40**, 441–465.
- , and —, 2010b: Numerical modeling of fetch-limited waves in the Gulf of Tehuantepec. *Phys. Oceanogr.*, **40**, 466–486.
- Snyder, R. L., and R. M. Kennedy, 1983: On the formation of whitecaps by a threshold mechanism. Part I: Basic formalism. *J. Phys. Oceanogr.*, **13**, 1482–1492.
- Stansell, P., and C. MacFarlane, 2002: Experimental investigation of wave breaking criteria based on wave phase speeds. *J. Phys. Oceanogr.*, **32**, 1269–1283.
- Steenburgh, W. J., D. M. Schultz, and B. A. Colle, 1998: The structure and evolution of gap outflow over the Gulf of Tehuantepec, Mexico. *Mon. Wea. Rev.*, **126**, 2673–2691.
- Stramska, M., and T. Petelski, 2003: Observations of oceanic white-caps in the north polar waters of the Atlantic. *J. Geophys. Res.*, **108**, 3086, doi:10.1029/2002JC001321.
- Stumpf, H. G., 1975: Satellite detection of upwelling in the Gulf of Tehuantepec, Mexico. *J. Phys. Oceanogr.*, **5**, 383–388.
- Sugihara, Y., H. Tsumori, T. Ohga, H. Yoshioka, and S. Serizawa, 2007: Variation of white-cap coverage with wave-field conditions. *J. Mar. Syst.*, **66**, 47–60.
- Sullivan, P. P., J. C. McWilliams, and W. K. Melville, 2004: The oceanic boundary layer driven by wave breaking with stochastic variability. Part 1. Direct numerical simulations. *J. Fluid Mech.*, **507**, 143–174.
- , —, and —, 2007: Surface gravity wave effects in the oceanic boundary layer: Large-eddy simulation with vortex force and stochastic breakers. *J. Fluid Mech.*, **593**, 405–452.
- Thomson, J., and A. T. Jessup, 2009: A Fourier-based method for the distribution of breaking crests from video observations. *J. Atmos. Oceanic Technol.*, **26**, 1663–1671.
- , J. R. Gemmrich, and A. T. Jessup, 2009: Energy dissipation and the spectral distribution of whitecaps. *Geophys. Res. Lett.*, **36**, L11601, doi:10.1029/2009GL038201.
- Thorpe, S. A., 1992: Bubble clouds and the dynamics of the upper ocean. *Quart. J. Roy. Meteor. Soc.*, **118**, 1–22.
- , 1993: Energy loss by breaking waves. *J. Phys. Oceanogr.*, **23**, 2498–2502.
- , and P. N. Humphries, 1980: Bubbles and breaking waves. *Nature*, **283**, 463–465.
- , and A. J. Hall, 1983: The characteristics of breaking waves, bubble clouds, and near-surface currents observed using side-scan sonar. *Cont. Shelf Res.*, **1**, 353–384.
- Tian, Z., M. Perlin, and W. Choi, 2008: Evaluation of a deep-water wave breaking criterion. *Phys. Fluids*, **20**, 066604, doi:10.1063/1.2939396.
- Toba, Y., 1973: Local balance in the air-sea boundary processes. III. On the spectrum of wind waves. *J. Oceanogr. Soc. Japan*, **29**, 209–220.
- Wu, J., 1975: Wind-induced drift currents. *J. Fluid Mech.*, **68**, 49–70.
- , 1979: Oceanic whitecaps and sea state. *J. Phys. Oceanogr.*, **9**, 1064–1068.
- , 1988: Variations of whitecap coverage with wind stress and water temperature. *J. Phys. Oceanogr.*, **18**, 1448–1453.
- Xu, D., X. Liu, and D. Yu, 2000: Probability of wave breaking and whitecap coverage in a fetch-limited sea. *J. Geophys. Res.*, **105** (C6), 14 253–14 259.
- Zhao, D., and Y. Toba, 2001: Dependence of whitecap coverage on wind and wind wave properties. *J. Oceanogr.*, **57**, 603–616.